The genetic driver of Acute Necrotizing Encephalopathy, *RANBP2*, regulates the inflammatory response to Influenza A virus infection

Sophie Desgraupes[1], Suzon Perrin[1], Benoît Gouy[1], Adrien Decorsière[1], Yifan E Wang[2], Alexander F. Palazzo[2], Sandie Munier[3], Nathalie J. Arhel[1*]

[1] Institut de Recherche en Infectiologie, University of Montpellier, CNRS UMR9004, 1919 route de Mende, 34090 Montpellier, France

[2] Department of Biochemistry, University of Toronto, 661 University Avenue, Toronto, ON M5G 1M1, Canada

[3] Institut Pasteur, Université Paris Cité, Unité Lyssavirus, Epidémiologie et Neuropathologie, F-75015, Paris, France

* Correspondence: nathalie.arhel@cnrs.fr

ABSTRACT

Influenza virus infections can cause severe complications such as Acute Necrotizing Encephalopathy (ANE), which is characterised by rapid onset pathological inflammation following febrile infection. Heterozygous dominant mutations in the nucleoporin RANBP2/Nup358 predispose to influenza-triggered ANE1. The aim of our study was to determine whether RANBP2 plays a role in IAV-triggered inflammatory responses. We found that the depletion of RANBP2 in a human airway epithelial cell line increased IAV genomic replication by favouring the import of the viral polymerase subunits, PB1, PB2 and PA, and promoted an abnormal accumulation of some viral segments in the cytoplasm. In human primary macrophages, this corroborated with an enhanced production of the pro-inflammatory chemokines CXCL8, CXCL10, CCL2, CCL3 and CCL4. Then, using CRISPR-Cas9 knock-in for the ANE1 disease variant RANBP2-T585M, we demonstrated that the point mutation is sufficient to drive CXCL10 expression following activation downstream of RIG-I and leads to a redistribution of RANBP2 away from the nuclear pore. Together, our results reveal that RANBP2 regulates influenza RNA replication and nuclear export, triggering hyper-inflammation, offering insight into ANE pathogenesis.

INTRODUCTION

Influenza viral infections are responsible for seasonal epidemics with respiratory manifestations but can also lead to severe complications. Among these, Acute Necrotizing Encephalopathy (ANE), also called ANE of Childhood (ANEC), is a severe reaction to febrile infection that is characterized by rapid progression and very poor prognosis (Lee et al., 2023; Sakuma et al., 2025; Wu et al., 2015; Mizuguchi et al., 2007). Influenza viruses are thought to be responsible for ~50% of all ANE episodes and are associated with high morbidity and mortality (Bartolini et al., 2024; Jiang et al., 2022; Mizuguchi et al., 2007; Neilson et al., 2003; Chatur et al., 2022; Bashiri et al., 2020). Although the pathogenesis is unclear, a hyperinflammatory response triggered by the virus is proposed as the underlying mechanism (Levine et al., 2020; Mizuguchi et al., 2007; Sugaya, 2002), and early anti-inflammatory therapy may help mitigate the disease (Chatur et al., 2022; Koh et al., 2019; Okumura et al., 2009).

Influenza viruses belong to the *Orthomyxoviridae* family and are classified into types, Influenza A and B being the most prevalent ones associated with seasonal flu cases. Influenza A is further divided into subtypes based on their surface glycoproteins, haemagglutinin (HA) and neuraminidase (NA). The H1N1 and H3N2 strains are responsible for major outbreaks and epidemics, and in the 2024-2025 winter

season, there has been an unprecedented surge in H1N1 cases, leading to an unusual spike in hospitalizations and ANE in children (Bartolini et al., 2024).

The Influenza A virus (IAV) is an enveloped particle containing 8 negative-sense single-stranded viral RNA (vRNA) gene segments, each packaged by nucleoprotein (NP) into a viral ribonucleoprotein (vRNP) complex, and associated with the viral polymerase complex (PB1, PB2, and PA). Unlike most RNA viruses, IAV replicates in the nucleus and hijacks the nuclear pore complex (NPC) machinery for four critical steps of its replication cycle. (i) After endocytosis and uncoating, vRNPs are trafficked to the nucleus where the viral polymerase transcribes the viral genome. (ii) Capped and polyadenylated mRNAs are exported into the cytoplasm for translation by cytoplasmic ribosomes. (iii) The newly translated viral proteins, including NP, PB1, PB2 and PA, are imported back into the nucleus, which allows the viral polymerase to replicate the viral genome into complementary RNAs (cRNA) and genomic vRNA. (iv) Lastly, new vRNPs, assembled with M1 and NS2/NEP, are exported back from the nucleus for incorporation into budding virions (Dou et al., 2018; Carter and Iqbal, 2024; Fodor and Te Velthuis, 2020; Zhu et al., 2023).

Many viral and host factors are thought to contribute to severe influenza, and genetic susceptibility particularly in genes that regulate innate signalling and antiviral response, has been reported (Mettelman and Thomas, 2021; Clohisey and Baillie, 2019; Gounder and Boon, 2019). However, the mechanisms that drive severe influenza-triggered ANE in previously healthy children are not known. One clue to understanding the pathogenesis of influenza-associated ANE comes from genetic susceptibility in familial, recurrent cases, known as ANE1 (or ADANE) (Neilson et al., 2003). Patients with ANE1 present with autosomal dominant missense mutations in *RANBP2* and have a significantly increased lifetime risk of developing ANE (Neilson et al., 2009). Mutations in *RANBP2* increase the risk of relapse and recurrence (Levine et al., 2020; Chatur et al., 2022) and may associate with greater morbidity and mortality.

RANBP2 (Nup358) is a cytoplasmic fibril (CF) nucleoporin that regulates nucleocytoplasmic transport by interacting with nuclear transport receptors such as Karyopherin α/β and CRM1/Exportin 1 (Yokoyama et al., 1995; Hutten et al., 2008). Additional functions have been attributed to RANBP2 at the NPC, many of which are linked to its C-terminal domain (CTD) E3 SUMO ligase activity, and away from the NPC, namely at annulate lamellae, mitochondria-endoplasmic reticulum junctions and in the nucleus (Desgraupes et al., 2023). Moreover, at least 4 protein isoforms have been identified for RANBP2, however, it is not known if these have distinct functions or subcellular localisations. The predominant ANE1-associated mutation (c.C1754T, p.T585M), and most other pathogenic mutations in RANBP2, all cluster in the N-terminal domain (NTD), which is responsible for anchoring to NPCs (Jiang et al., 2022; Joseph and Dasso, 2008). This suggests that the localization of RANBP2 to CF may be physiologically essential, although no changes in localisation could be demonstrated following the overexpression of disease variants (Shen et al., 2021; Bley et al., 2022).

Previous work showed that RANBP2 can modulate viral infection of several viruses, such as Adenovirus (Carlon-Andres et al., 2020), Herpes simplex virus type 1 (HSV-1) (Copeland et al., 2009; Hofemeister and O'Hare, 2008) and Human immunodeficiency virus type 1 (HIV-1) (Bichel et al., 2013; Di Nunzio et al., 2012; Schaller et al., 2011; Zhang et al., 2010), however no work has uncovered a role for RANBP2 in Influenza virus infection. In fact, although some studies showed that NPC components can impact the replication and transcription of Influenza virus, such as Nup62, Nup98 and Nup153, RANBP2 was not identified as a host factor for Influenza virus (Khanna et al., 2024; Watanabe et al., 2010; Munier et al., 2013).

Previous work also showed that RANBP2 can modulate innate immune signalling, however this activity was consistently attributed to its E3 SUMO ligase activity or Cyclophilin-homology motif in the CTD

(Maarifi et al., 2018; Portilho et al., 2016; Shen et al., 2021; Li et al., 2023), and no work has yet demonstrated a role for the NTD where ANE1 mutations are clustered.

The aim of our study was to determine how RANBP2 contributes to or regulates inflammatory responses to infection by Influenza virus. We show that RANBP2 impacts the replication of genomic vRNAs of IAV into cRNA by controlling the re-import of newly translated viral polymerase complex. Interestingly, RANBP2 also controls RNP export from the nucleus but in a segment-specific manner, only impacting the long segments encoding the PB1, PB2 and PA proteins, thus leading to their cytoplasmic accumulation and triggering hyper-inflammation, which could provide a first clue in understanding the pathogenesis of ANE.

RESULTS

Knockdown of RANBP2 stimulates non-productive Influenza vRNA replication in infected cells

To investigate the role of RANBP2 in IAV infection, RANBP2-knockdown (RANBP2-KD) was induced in A549 human alveolar cells by lentiviral vector (LV) transduction before infection with A/WSN/1933(H1N1) virus at MOI 0.5. Supernatants were harvested at 10 h post-infection (hpi) to investigate the production of infectious viral particles by TCID50 titration. No differences were observed between the Control and RANBP2-KD cells, suggesting that RANBP2 had no effect on the production of infectious particles **(Figure 1A, Figure S1)**.

However, an unexpected phenotype was observed for viral RNA quantification in both A549 and the monocytic cell line THP-1. Infection kinetics were performed and viral RNA levels were determined at early (2 h) and late (6, 8, 16 and 24 h) time points using qPCR primers recognizing M1 on segment 7. In the monocytic cell line THP-1 **(Figure 1B)** and in A549 cells **(Figure 1C)**, a significant increase of M1 RNA was induced in RANBP2-KD cells. Although the change was most striking in THP-1 cells (40-fold), this led to considerable cell death and, therefore, A549 cells were preferred for further analysis. The increase in viral RNA was confirmed with another IAV segment, encoding the NP **(Figure 1D)**, and appeared to be specific since no increase was observed for any of the housekeeping genes that were measured **(Figure 1E)**. Together, these data suggested that RANBP2 is involved in controlling Influenza viral RNA synthesis but that this does not translate into increased productive infection.

Because different types of viral RNAs are produced during the IAV life cycle, we investigated which RNAs are impacted by the depletion of RANBP2. Tagged RT primers were used to specifically recognize the negative-sense genomic vRNA sequence or the positive-sense cRNA sequence in order to specifically reverse transcribe (RT) each type of viral RNA **(Figure S2A)**. First, the specificity of each primer was validated by amplifying only vRNAs after vRNA-specific RT, or only cRNAs after cRNA-specific RT, while not amplifying any target in non-infected cells **(Figure S2B)**. In RANBP2-KD cells, we observed a significant increase of both vRNAs and cRNAs **(Figure 1F)**, thus showing that RANBP2 is involved in IAV RNA replication. Although this was unexpected given the absence of phenotype in terms of viral production, the marked increase in cRNA and vRNA levels suggested an enhancement in viral genome replication.

Having observed an increase in genomic vRNAs, we tested if this correlated with more newly produced vRNPs. As previously, A549 cells were transduced with Control- or RANBP2-shRNAs then infected with IAV (MOI 0.5). At 8 hpi, the distribution of NP was investigated by immunofluorescence. Although export is ongoing in every condition, RANBP2-KD cells showed a striking increase in cytoplasmic NP **(Figure 1G and 1H, Figure S3).** In order to determine if signal corresponded to vRNPs or free NP in the cytoplasm, we performed co-stainings with other components of vRNPs (i.e. PB1 and PA). We observed a co-localisation of cytoplasmic NP with PB1 and with PA **(Figure 1I and 1J, Figure S4)**, showing that RANBP2-KD induces an increase in vRNPs exported to the cytoplasm.

Increased IAV replication does not result from enhanced viral entry into cells or into the nucleus

To determine how vRNA is increased in RANBP2-depleted cells, we first tested whether RANBP2 regulates IAV infection by modulating viral entry into cells and/or nuclei, thereby increasing the quantity of IAV RNA to be copied.

To assess whether RANBP2 regulates cell or nuclear entry, Control or RANBP2-KD cells were infected with IAV (A/WSN/33) at MOI 4 in order to increase signal detection during early steps of the viral cycle, and NP localization was studied by immunofluorescence at 1 hpi to assess internalization, and at 2 h to monitor NP nuclear entry. Results indicate that depletion of RANBP2 from A549 cells affects neither internalization **(Figure 1K and 1L)** nor nuclear import **(Figure 1M and 1N)**.

To further validate these findings, we adapted an Alpha-Centauri protein-complementation assay previously developed to monitor the nuclear import of HIV-1 (Fernandez et al., 2021). Briefly, the NanoLuc protein was expressed as two unequal non-luminescent fragments. The smaller fragment was fused to PB2 (called Alpha), while the larger fragment (Centauri) was fused to a NLS and expressed in A549 cells by lentiviral vector (LV) transduction **(Figure 1O, Figure S5A and S5B)**. Upon vRNP nuclear import, the two fragments reconstitute a functional NanoLuc, generating a measurable signal upon addition of substrate **(Figure S5C)**. No significant differences in luminescence were detected between control and RANBP2-KD cells at 1 and 2 hpi, confirming that RANBP2 is not essential for vRNP nuclear import **(Figure 1P, Figure S5D)**, thus demonstrating that RANBP2 does not regulate IAV vRNP nuclear import.

RANBP2 Knockdown facilitates the nuclear import of the neo-synthesised viral polymerase complex proteins PB1, PB2 and PA

Since RANBP2 does not impact the quantity of template available for replication, we investigated whether it modulates the quantity or transport of the polymerase complex subunits. First, the total levels of PB1, PB2, PA and NP were assessed by Western-Blot at 8 hpi, however, no differences were observed between RANBP2-KD cells and Control cells **(Figure 2A)**, suggesting that RANBP2 does not impact the translation of the viral polymerase complex.

Being an NPC component, we hypothesised that RANBP2 may control the replication of vRNA by regulating the import of the viral polymerase. Therefore, we tested the impact of RANBP2 on the nuclear import of newly synthesised PB1, PB2, and PA subunits. To focus specifically on import, we inhibited vRNP export using a pharmacological inhibitor of CRM1, KPT-330/Selinexor. First, we confirmed that KPT-330 inhibits vRNP export in a dose-dependent manner **(Figure S6A)**, with negligible toxicity **(Figure S6B)** and that inhibition operates from 5 hpi onwards **(Figure S6C)**. Then we performed subcellular fractionation followed by Western blotting at 6 hpi to determine the localisation of the different polymerase subunits. Results revealed an increase in PB1, PB2 and PA protein levels in the nucleus, confirmed by the immunofluorescence detection of nuclear PB1, indicating that the import of the neo-synthesised polymerase is facilitated in the absence of RANBP2 **(Figure 2B and 2C, Figure S7)**.

RANBP2 depletion disrupts the segment stoichiometry by selectively favouring the export of some vRNA segments to the cytoplasm

Having determined that RANBP2 controls Influenza virus replication in the nucleus by regulating the import of the newly synthesised viral polymerase, we asked why the increase in vRNA and vRNP does not translate into an increased production of infectious particles **(Figure 1A)**. To address this, we performed strand-specific RT to distinguish vRNA and cRNA, as previously **(Figure S2A)**, then quantified the 8 IAV segments by qPCR to investigate segment stoichiometry **(Figure 2D, Figure S8A and S8B)**. After sub-cellular fractionation, analysis of viral RNA localization revealed that, while cRNA levels increased for all

177 influenza segments in the nucleus **(Figure 2E)**, segments 1, 2, 3, 7 and 8 exhibited increased vRNA export
178 to the cytoplasm in the absence of RANBP2 compared to other segments **(Figure 2F)**. These findings
179 indicate that, while the depletion of RANBP2 increases the replication of all vRNA segments, it
180 disproportionately affects their export back to the cytoplasm.

181 Taken together, our results indicated that the knockdown of RANBP2 greatly perturbs infection by IAV,
182 first by facilitating the re-import of polymerase into the nucleus, which increases cRNA and vRNA, second
183 by selectively favouring the export of some vRNA into the cytoplasm. The dysregulation of both these
184 steps may cause an abnormal accumulation of some vRNA segments in the cytoplasm, thus constituting
185 potential pathogen-associated molecular patterns (PAMPs) that may be sensed by the infected cell.

186 **RANBP2 knockdown exacerbates the inflammatory response to IAV infection in primary human**
187 **macrophages**

188 In ANE1, it is thought that innate immune cells may contribute to the deleterious production of cytokines
189 following IAV infection. To test this in relevant innate immune cells, primary monocytes were isolated
190 from PBMCs from healthy donors and differentiated into pro-inflammatory M1-like macrophages. After
191 7 days of differentiation, primary monocyte-derived macrophages (MDM) were CD3- CD14+ CD16+
192 CD11b+ HLA-DR+ CD80- **(Figure S9)**. We first determined that IAV can infect MDMs **(Figure S10A)**, and
193 stimulate an effective immune response without additional pre-stimulation, triggering the synthesis of
194 pro-inflammatory cytokines such as IL-6 and IL-1β **(Figure S10B)**. MDM were then transduced with LVs
195 coding for control or RANBP2 shRNA and infected with IAV **(Figure S1)**. The stimulation of innate
196 immunity was initially assessed by qPCR detection of representative transcripts, namely CXCL10, IL-6,
197 TNFα and IL-1β, comparing MDM with THP-1 and A549 cells. Although some cell-dependent changes
198 were observed, the knockdown of RANBP2 led to a ~2-fold increase in IL-6, up to 6-fold increase in TNFα
199 and IL-1β, and up to 50-fold increase in CXCL10 **(Figure 3A)**, suggesting that RANBP2 regulates the
200 inflammatory response to IAV infection.

201 To confirm this at the protein level, supernatants were collected at 24 hpi and the secretion of pro-
202 inflammatory mediators was analysed by Multiplex Luminex assay. Strikingly, the knock-down of RANBP2
203 in primary macrophages led to an exacerbated inflammatory response to IAV infection, with a stronger
204 induction of the pro-inflammatory chemokines CXCL8, CXCL10, CCL2, CCL3 and CCL4 **(Figure 3B)**.

205 Together, these findings suggest that RANBP2 plays a critical role in modulating the inflammatory
206 response to IAV infection by regulating vRNA replication, nucleocytoplasmic trafficking of viral
207 polymerase subunits, and selective vRNA export. The abnormal accumulation of viral components in the
208 cytoplasm amplifies inflammatory signalling, highlighting a potential mechanism underlying the
209 pathogenesis of ANE.

210 **The RANBP2-T585M ANE1 variant drives hyper-inflammation following IAV infection**

211 Having identified the role of RANBP2 in controlling the IAV-triggered inflammation, we investigated if
212 this function is compromised by the predominant ANE-associated mutation, c.C1754T, p.T585M.
213 Heterozygous mutations in *RANBP2* are associated with increased susceptibility to acute necrotizing
214 encephalopathy, however it is not known how these affect protein function. In particular, previous work
215 showed that ANE1 mutations do not alter the structure of RANBP2 (Bley et al., 2022), and that
216 ectopically-expressed RANBP2-T585M still localises to the nuclear envelope (Bley et al., 2022; Shen et al.,
217 2021).

218 We introduced the predominant mutation (c.C1754T, p.T585M), by CRISPR-Cas9 knock-in of U2OS cells
219 **(Figure 4A)**. A total of 47 clones were isolated after puromycin selection during 3 weeks. Mutations were
220 confirmed by allelic qPCR **(Figure 4B, Figure S11A-S11C),** as previously described (Gouy et al., 2023), and

by Sanger sequencing of the cDNA **(Figure 4C and 4D)**. For many clones, we noted that CRISPR repair had occurred using the highly homologous RGPD sequences present on the same chromosome (Desgraupes et al., 2023), rather than the repair plasmid, therefore only clones that did not recombine with RGPD were selected **(Figure S11B)**. In total, two wild-type clones (C4 and C15, referred to as WT/WT), one heterozygously-mutated (C10, WT/C1754T) and three homozygously-mutated (C6, C9 and C14, C1754T/ C1754T) clones were isolated.

CRISPR-knock-in clones were infected with IAV and activation of innate immune pathways was assessed by qPCR, normalised for house-keeping genes, as previously **(Figure 3A)**. IAV infection induced expression of CXCL10 and TNFα transcript expression in all clones. However, a striking phenotype emerged in cells homozygous for the RANBP2-T585M disease variant, where CXCL10 expression following IAV infection was exacerbated by a fold change of 1-2-log compared to WT or heterozygous clones **(Figure 4E).** A similar phenotype was observed upon transfection of the constitutively active caspase recruitment domain (2-CARD) of the retinoic acid-inducible gene I (RIG-I), which mimics viral RNA sensing (Maarifi et al., 2018), suggesting that the ANE1-associated variant amplifies innate immune responses to agonist stimulation.

In CRISPR-Cas9 knock-in cells, RANBP2 mislocalises away from nuclear pores

Although previous studies reported that ectopically expressed RANBP2-T585M localizes to the NPC (Bley et al., 2022; Shen et al., 2021), its localization has not been examined in genetically edited cell lines. We therefore examined the subcellular localisation of RANBP2 by immunofluorescence in the clones expressing RANBP2-T585M heterozygously and homozygously using a RANBP2-specific antibody recognising the CTD. As expected, RANBP2 localised to the nuclear envelope in WT clones. In contrast, all three clones homozygous for RANBP2-T585M lost the characteristic nuclear rim staining, indicating that the mutation disrupts RANBP2 retention at the nuclear envelope **(Figure 4F-4H)**. Despite this, nuclear pores appeared intact, since the labelling of FG-repeat Nups with the MAb414 antibody was comparable across all clones **(Figure 4F, Figure S12)**.

In conclusion, our findings suggest that RANBP2 localization at the nuclear envelope is critical to safeguard cells from the pathological inflammation following viral infection. In ANE1, mutations in the NTD of RANBP2 are specifically associated with hyperinflammation.

DISCUSSION

In this work, we show that the NPC component RANBP2 regulates the nucleocytoplasmic transport of Influenza A virus proteins and RNAs. Its absence from nuclear pores contributes to exacerbated viral replication in the nucleus, and a disproportionate increase in some viral RNAs. While previous work indicated that RANBP2 is a co-factor for the infection by some viruses (Bichel et al., 2013; Di Nunzio et al., 2012; Schaller et al., 2011; Zhang et al., 2010; Copeland et al., 2009; Hofemeister and O'Hare, 2008), this study reveals an opposite role in IAV infection, namely the restriction of key nuclear transport steps.

RANBP2 can regulate the nucleocytoplasmic transport of macromolecules by two major mechanisms, first by regulating the cycle of Ran, second by interacting with nuclear transport receptors (Yokoyama et al., 1995; Hutten et al., 2008). The replication of IAV involves four distinct sequential NCT steps, namely the import of incoming vRNPs, the export of viral mRNAs, the import of translated viral proteins, and the export of vRNPs. RANBP2 was found to regulate only two of these steps, suggesting a specific mechanism. In particular, RANBP2 was not involved in the initial entry of incoming vRNPs into the nucleus, which involves the classical karyopherin α/β nuclear import pathway (Miyake et al., 2019; Nguyen et al., 2023; Dou et al., 2018), nor in the initial export of viral transcripts, which involves the general mRNA export pathway via NXF1:NXT1. Rather, RANBP2 acted on late nuclear transport steps of IAV, after translation of the viral proteins. First, RANBP2 was found to regulate the re-import of the

polymerase complex subunits, which is known to involve different pathways, the best characterised being via the β-karyopherin RanBP5 (Huet et al., 2010; Hemerka et al., 2009; Cros et al., 2005). Second, results suggest that RANBP2 exerts a quality control checkpoint for vRNAs that are exported back to the cytoplasm, a step known to depend on the β-karyopherin CRM1 (Elton et al., 2001; Ma et al., 2001; Watanabe et al., 2001). Our results therefore suggest that RANBP2 may impact viral NCT by interacting with key β-karyopherins.

Despite increased vRNA levels, infectious viral particle production did not increase. Our results indicated that the absence of RANBP2 disrupted the segment stoichiometry, leading to the disproportionate increase in the largest segments (1, 2, 3), and in segments that undergo splicing (7 and 8). Changes in segment stoichiometry could lead to packaging defects, however, the mechanism responsible for this imbalance in viral RNA export is not known. It is possible that the increase in vRNA corresponds to truncated RNA segments, especially since large deletions are frequent in the segments coding for PB1, PB2 and PA.

After replication, Influenza viral genomic single stranded RNA molecules are sensed by RIG-I, which results in the production of pro-inflammatory cytokines downstream of NF-κB (Iwasaki and Pillai, 2014). In the absence of RANBP2, IAV infection led to a dramatic increase in the pro-inflammatory response, especially with the production of chemokines. We hypothesize that the disproportionate increase of some cRNA/vRNA segments in the cytoplasm could constitute PAMPs that exacerbate the inflammatory response.

Influenza viruses are responsible for the majority of ANE1 cases in children. The high prevalence for Influenza over other respiratory infections (e.g., RSV, SARS-CoV-2) and childhood febrile illnesses (e.g., streptococcal infections) is puzzling and unexplained. Our work suggests that, by restraining key steps of IAV nucleocytoplasmic trafficking, RANBP2 is responsible for limiting the accumulation of viral PAMPs in the cytoplasm. Additionally, in CRISPR knock-in cells expressing the ANE1 disease variant, stimulation of innate immune signalling downstream of RIG-I led to a high expression of some pro-inflammatory transcripts, indicating that RANBP2 also regulates innate immune signalling. Although the prevalent phenotype was observed in homozygously edited cells, this is the first demonstration that ANE1 mutation is associated with exacerbated inflammation. This role of RANBP2 in controlling innate immunity is coherent with the symptoms observed in ANE1 patients as they express elevated levels of pro-inflammatory cytokines.

It remains unclear how heterozygous dominant single point mutations in the NTD of RANBP2 contribute to disease. Previous work suggests that both wild-type and mutant alleles are expressed in patients (Gouy et al., 2023), suggesting that the mutant allele might have dominant negative activity. However, ANE1 mutations were shown not to affect protein structure, nor localisation at the NPC using ectopically-expressed RANBP2 (Bley et al., 2022; Shen et al., 2021). In CRISPR knock-in cells, we demonstrate that the T585M mutation in the NTD causes its redistribution away from the nuclear envelope. This change was only observed in homozygously-edited cells, suggesting that the mutation affects the ability of mutant-RANBP2 to anchor into the NPCs. Future work in patient samples will be essential to determine whether ANE1 mutations favour the accumulation of RANBP2 isoforms or truncated forms.

MATERIALS & METHODS

Viruses, lentiviral vectors and cells

Infections with IAV were carried out with the H1N1/A/WSN/1933 strain in all experiments except for the Alpha-Centauri assay where this same strain was engineered to express a fragment of the NanoLuc (IAV-

alpha) as described below. Lentiviral vectors (LV) were produced by transfecting HEK-293T cells in calcium phosphate with a pVSVg plasmid, an encapsidation Gag-Pol plasmid (p8.74) and the plasmid of interest (i.e. mCherry-shRNA-Control, mCherry-shRNA-RANBP2 or Centauri-NLuc-NLS) (see **Table S1** for plasmid information). After 48 h, vectors were harvested and ultracentrifuged for 1 h at 22,000 rpm (Optima XE-90, Beckman Coulter) at 4°C. A549 cells (ATCC) and CRISPR U2OS clones (homemade) were cultured in Dulbecco's Modified Eagle Medium (DMEM, Gibco) containing 10% of Fetal bovine serum (FBS, Serana) and 1× penicillin/streptomycin (PS, Gibco) at 37°C with 5% CO2. THP-1 cells and monocyte-derived macrophages (MDM) were cultured in Roswell Park Memorial Institute (RPMI-1640, Gibco) medium containing 10% FBS and 1× of PS.

IAV infections

Cells were infected with IAV at MOI 0.5 in all experiments, except when monitory the early steps of the viral cycle (i.e. internalization, nuclear import), when MOI 4 was used to increase signal detection. Cells were exposed to IAV for 1 h in a small volume of 2% FBS culture medium to promote viral adsorption at the cell surface before replacing viral inoculum with warm culture medium and incubation at 37°C with 5% CO2. For experiments with NF-κB canonical pathway inhibition, cells were pre-treated with 2% FBS culture medium containing 20 µM of PS1145 (MedChemExpress) for 1 h at 37°C.

RNA extractions and RTqPCR

Intracellular RNAs were extracted using the RNeasy mini kit (Qiagen) according to the manufacturer's protocol. RNA yields and purity were assessed by spectrophotometry (NanoDrop 2000c, Thermofisher Scientific). Unspecific reverse transcription (RT) was performed using the PrimeScript RT Reagent Kit (Perfect Real Time, Takara Bio Inc.) with random and polyT primers. IAV strand-specific RT was performed using tagged primers that bind either to the consensus 3'-end sequence of vRNAs (all 8 segments) or to the consensus 3'-end sequence of cRNAs (all 8 segments as well) with Superscript III (Invitrogen, Thermofisher Scientific) in the presence of DTT 0.1M (Invitrogen, Thermofisher Scientific), dNTP 10mM (Invitrogen, Thermofisher Scientific) and RNAsin (Promega). Distinction between segments was then made using specific qPCR primers (**Table S2**). RANBP2-specific RT was performed using a primer (at 1µM) that binds to RANBP2 on a sequence absent from RGPDs, as published in (Gouy et al., 2023) PrimeScript RT Reagent Kit was used (Perfect Real Time, Takara Bio Inc.) (**Table S2**). Real-time quantitative PCR was performed using the Power Up kit (Applied Biosystems, Thermofisher Scientific) on the ViiA7 thermocycler (Life technologies, Thermofisher Scientific). All qPCR primers are listed in **Table S2**.

Immunofluorescence

Cells were washed with PBS and fixed with 4% paraformaldehyde (PFA, Thermofisher Scientific) for 10 min at room temperature (R/T). After 3 PBS washes, remaining PFA was neutralized with PBS containing 50mM of NH4Cl for 10 min at R/T. After 2 PBS washes, cells were permeabilized using PBS containing 0.5% of Triton-100X (Sigma-Aldrich) for 15 min at R/T. Cells were washed twice in PBS and saturated in PBS supplemented with 2% of Normal goat serum (NGS, Invitrogen, Thermofisher Scientific). Primary stainings were performed for 1h at R/T with antibodies listed in **Table S3**. Cells were washed 5 times with PBS and secondary antibodies were added for 30 min at R/T (**Table S3**). After 5 PBS washes, cells were stained with Hoechst (Thermofisher Scientific) diluted to the 1/10,000 in PBS for 5 min at R/T. Cells were washed 5 times with PBS and mounted in Prolong Diamond anti-fade mounting medium (Invitrogen, Thermofisher Scientific). Imaging was carried out using the Confocal Zeiss LSM880 Airyscan microscope of the Montpellier Ressources Imagerie (MRI) platform. Image processing and quantifications were done using the Fiji software (2.14.0): Alexafluor-488 staining of the NP was changed to the color « Orange

354 Hot » for aesthetic purposes and brightness was increased uniformly in all conditions. Full panels of
355 images are provided in supplementary data.

356 **Alpha-Centauri assay**

357 Cloning steps. A DNA fragment coding for αNluc (GVTGWRLCERILA) flanked by NotI and NheI overhangs
358 was obtained by annealing two overlapping oligonucleotides:

NotI-αNLuc-NheI-F GGCCGCAGGGGGAGTGACAGGGTGGAGACTATGCGAAAGAATACTTGCATAAG

NotI-αNLuc-NheI-R CTAGCTTATGCAAGTATTCTTTCGCATAGTCTCCACCCTGTCACTCCCCCTGC

359 The reverse genetics plasmid pPolI-SL-PB2-αNluc was obtained by subcloning this restriction fragment
360 between the NotI and NheI sites of the pPolI-SL-PB2-Nanoluc described in Diot 2016.

361 Particle production by reverse genetics. The eight pPolI-WSN-PB2-αNluc, -PB1, -PA, -HA, -NP, -NA, -NS, -
362 M, and four pcDNA3.1-WSN-PB2, -PB1, -PA, -NP plasmids (0.5 µg of each) were co-transfected into a co-
363 culture of 293T and MDCK cells (seeded in a 6-well plate at 4×10^5 and 3×10^5 cells, respectively) using
364 10 µL of FuGENE® HD transfection reagent (Promega). After 24 h of incubation at 35°C, cells were
365 washed twice with DMEM and incubated in DMEM containing 1 µg/mL of TPCK-treated trypsin for 48 h.
366 The reverse genetics supernatant was titrated on MDCK by plaque assay and the recombinant PB2-αNluc
367 virus was amplified at an MOI of 10^{-4} on MDCK cells for 3 days at 35°C. The viral stock was titrated on
368 MDCK by plaque assays and sequenced to verify the presence of the αNluc coding sequence.

369 Cells were transduced with LV Centauri-NLuc-NLS for 3 days, then with LV shRNA-Control or LV shRNA-
370 RANBP2 at MOI 15 for 4 days. Cells were then infected with IAV-α at MOI 4 for the indicated times.
371 NanoGlo live cell substrate (Promega) was added and luminescence was measured with the Infinite M
372 Plex spectrophotometer (Tecan).

373 **Nucleo-cytoplasmic fractionation**

374 Nuclear and cytoplasmic fractions were separated using the NE-PER Kit (Thermofisher Scientific)
375 according to the manufacturer's protocol. Briefly, 1-2 million cells were washed with PBS then lysed in
376 cold CER I buffer, vortexed 15 seconds and incubated on ice for 10 min. Cold CER II buffer was then
377 added and cells were vortexed 5 seconds then incubated on ice for 1 min. After 5 second vortex and full
378 speed centrifugation, supernatants (cytoplasmic fraction) were harvested and stored at -80°C. Pellets
379 (nuclei) were resuspended in cold NER buffer and 4 cycles of 15 second vortex then 10-min incubation
380 on ice were performed. After full speed centrifugation, supernatants (nuclear fraction) were harvested
381 and stored at -80°C.

382 **Western blot**

383 Cell lysates were sonicated for 20 cycles of 30 seconds ON, 30 seconds OFF (Bioruptor Pico, Diagenode)
384 and 4X Laemmli (250 mM Tris-HCl pH 7, 8% sodium dodecyl sulphate (SDS), 40% glycerol, 10% β-
385 mercaptoethanol and 0.005% bromophenol blue) was added. After denaturation at 95°C for 5 min,
386 samples underwent SDS polyacrylamide gel electrophoresis (SureCast Gel Handcast System, Thermo
387 Fisher Scientific) and were transferred on a 0.45 µm nitrocellulose membrane (Sigma Aldrich).
388 Membranes were saturated in PBS containing 0.05% Tween 20 (Sigma) and 10% milk powder for 30 min.
389 Primary antibodies were added and left overnight at 4°C (**Table S3**). After 3 PBS washes, secondary
390 antibodies were added for 1 h at R/T (**Table S3**). Protein revelation was carried out by measuring HRP
391 activity (Immobilon Forte Western HRP substrate, Merck) with a Chemidoc imager (Biorad).

392 **TCID50 assay**

393 MDCK cells were washed in FBS-free MEM medium (Gibco) and serially diluted cell supernatants were
394 added in 2% FBS in octoplicates. After 3 days at 37°C and 5% CO2, cells were washed twice in PBS and
395 fixed with 4% PFA for 10 min at R/T. Violet crystal was added, washed twice in water and cytopathic
396 effect was observed. The TCID50 titer was determined using the formula:

397 log10 (TCID50/mL) = x0 - (d/2) + (d*xi/n) + v

398 x0: decimal logarithm of initial dilution factor.

399 d: decimal logarithm of serial dilution factor.

400 xi: score of positive events.

401 n: number of replicates.

402 v: decimal logarithm of the inoculum volume (mL).

403 **Peripheral blood mononuclear cell (PBMC) isolation**

404 Buffy coats from healthy donors were obtained from the Établissement Français du Sang (EFS). Whole
405 blood was diluted by half with Phosphate buffered saline (PBS) and loaded on an equivalent volume of
406 Lymphoprep (Stemcell technologies) at R/T. Tubes were centrifuged at 800g for 30 min at 20°C without
407 brakes. The PBMC ring was collected using a 5 mL pipet and washed 3 times in a final volume of 50 mL of
408 PBS (centrifugations at 1200 rpm for 5 min at 20°C with brakes on). The cell pellet was resuspended in 30
409 mL of 10% FBS RPMI-1640 medium. PBMCs were counted manually using counting chambers (Kova).

410 **Monocyte-derived macrophages differentiation**

411 After PBMC isolation, 20 million cells were seeded per well into 6-well plates and incubated for 45 min,
412 at 37°C with 5% CO2. After monocyte adherence, cells were washed 3 times with 10% FBS RPMI-1640
413 medium directly on the cell layers to remove non-attached cells. For monocyte-derived macrophage
414 (MDM) differentiation, monocytes were cultured in 10% FBS RPMI-1640 medium containing GM-CSF (50
415 ng/mL, Gentaur) for 8 days.

416 **Flow cytometry phenotyping**

417 After 8 days of MDM differentiation, phenotypic markers were analysed by flow cytometry on a Fortessa
418 using the following antibodies: CD3-BV421 (clone UCHT1, Biolegend 300433), CD14-PerCP-Cy5.5 (clone
419 HCD14, Biolegend 325621), CD16-Alexa700 (clone 3G8, Biolegend 302026), CD11b-APC-Cy7 (clone
420 M1/70, Biolegend 101225), HLA-DR-FITC (REA805, Miltenyi 130-111-941), and CD80-BV650 (clone 2D10,
421 Biolegend 305227).

422 **Multiplex LUMINEX assay**

423 The presence of mediators of inflammation was assessed in supernatants of stimulated cells using the
424 ProcartaPlex Human inflammation Panel 20-plex kit (Invitrogen, ThermoFisher Scientific). A few samples
425 were centrifuged and diluted to the 1/10 or to the 1/50 in order to determine optimal dilution for the
426 experiment. Dilution to the 1/50 was chosen to detect the strongly induced mediators (e.g. IL-8) in the
427 range of the standard curves supplied in the kit. Buffers and standards were prepared according to the
428 manufacturer's protocol. Briefly, Capture Bead mix was vortexed and added to the plate, washed in
429 Wash buffer, then samples and standards were added. The plate was incubated 1 h at R/T on a shaker.
430 After 2 washes, Biotinylated Detection Antibody mix was added for 30 min at R/T on a shaker. After 2
431 washes, Streptavidin-PE was added for 30 min at R/T on a shaker. After 2 more washes, the plate was
432 read on the MAGPIX flow cytometer (LUMINEX).

433 **Establishment of U2OS clones expressing RANBP2 T585M by CRISPR knock-in**

The plasmid pUclDT Amp (synthetized by Integrated DNA Technologies) containing the donor sequences (see below) and the plasmid pSpCas9(BB)-2A-Puro (PX459) (Addgene #62988) modified to contain the guide sequences (GGCAGAATGCCTTCAGAAAA) were co-transfected at equal quantity in the human osteosarcoma cell lines U2OS using Lipofectamine 3000 (Invitrogen, ThermoFisher Scientific) following the manufacturer's instructions. Two days post-transfection, cells were selected using puromycin (Gibco) at 2µg/ml during four days. The different clones were established by limiting dilution. A total of 198 cells were split in 576 different wells containing 10% FBS DMEM medium. After 3 weeks, 47 clones were established and analyzed by RANBP2-specific RTqPCR as describe above and Sanger sequencing (Eurofins).

<u>Donor DNA sequence</u>:

(GCGGTTTGTACTCTGATTCACAGAAAAGCAGTgtaagtagtaaaacaaaaatattgctttcacttagtgcgtaggttttaccggggattt
aatcctcatgtgaagatttaatttgtcatgtgacccattaacatatatgtatgtaagccctgaactgtgtatttagaaagcaattttagtaaattgaactat
tttttagACCTGGAAACGTAGCAAAATTGAGACTTCTAGTTCAGCATGAAATAAACACTCTAAGAGCCCAGGAAAAAC
ATGGCCTTCAACCTGCTCTGCTTGTACATTGGGCAGA<u>g</u>TG<u>t</u>CT<u>g</u>CAGAAAA**<u>t</u>**Ggtgagttttaaagtataagcatttttaaagaa
cattaccttaattttttaaaatcatgaactttttattgaaagtttttttgttctgaaaacagcagcttggtcacattatgacagatgtgtttttttattgctgca
aaatagttaatgtagttaaatataagcacttagaggagcaatgcctggcacacagtgaatgttacatattagctgagctgttactgttattccttaataat
taagttctgataattattcagcctgaaaattaaaaaaa)

Capital letters: exon

lowercase: intron

underlined: mutations

Bold lowercase: C1754T mutation

Generation of homozygous/heterozygous RANBP2-expressing control cells for allelic qPCR

HEK-293T cells were transfected with plasmids encoding the mCherry-RanBP2-shRNA and either GFP-RANBP2-WT, GFP-RANBP2-T585M or both (**Table S1**) in calcium phosphate. After 48 h of culture, cells were detached using trypsin (Gibco) and sorted on the ARIA IIu cytometer (Becton Dickinson) of the MRI platform to isolate the mCherry-positive cells. Sorted cells were lyzed and total RNAs were extracted using the RNeasy mini kit (Qiagen) according to the manufacturer's protocol.

Statistical analysis

Statistical analysis was performed using the GraphPad Prism software (10.2.3).

ACKNOWLEDGMENTS

This work was financed by grants from the Agence Nationale de la Recherche (ANR-23-CE15-0005-01) and ANRS-MIE (ECTZ209411). We thank Marion Cannac (Université de Montpellier, France) for help with phenotyping primary macrophages, and Montpellier Ressources Imagerie (MRI) for support with flow cytometry, cell sorting and imaging. We thank Rick Wozniak (University of Alberta, Canada) for the kind gift of RANBP2-specific antibody, Jomon Joseph (National Center for Cell Science, Pune, India) for the GFP-RANBP2 construct, and Sébastien Nisole (INSERM) for the GFP-RANBP2-T585M construct.

REFERENCES

Bartolini, L., S. Ricci, C. Azzari, M. Moriondo, F. Nieddu, M. L'Erario, Z. Ricci, G. Simonini, M. Mortilla, G. Indolfi, C. Montagnani, E. Chiappini, L. Galli, and R. Guerrini. 2024. Severe A(H1N1)pdm09 influenza acute encephalopathy outbreak in children in Tuscany, Italy,

December 2023 to January 2024. *Eurosurveillance*. 29. doi:10.2807/1560-7917.ES.2024.29.17.2400199.

Bashiri, F.A., S. Al Johani, M.H. Hamad, A.Y. Kentab, A.H. Alwadei, K. Hundallah, H.H. Hasan, W. Alshuaibi, L. Jad, M.T. Alrifai, A. Hudairi, R. Al Sheikh, A. Alenizi, N.A. Alharthi, T.A. Abdelmagid, D. Ba-Armah, M.A. Salih, and B. Tabarki. 2020. Acute Necrotizing Encephalopathy of Childhood: A Multicenter Experience in Saudi Arabia. *Front. Pediatr.* 8:526. doi:10.3389/fped.2020.00526.

Bichel, K., A.J. Price, T. Schaller, G.J. Towers, S.M. Freund, and L.C. James. 2013. HIV-1 capsid undergoes coupled binding and isomerization by the nuclear pore protein NUP358. *Retrovirology*. 10:81. doi:10.1186/1742-4690-10-81.

Bley, C.J., S. Nie, G.W. Mobbs, S. Petrovic, A.T. Gres, X. Liu, S. Mukherjee, S. Harvey, F.M. Huber, D.H. Lin, B. Brown, A.W. Tang, E.J. Rundlet, A.R. Correia, S. Chen, S.G. Regmi, T.A. Stevens, C.A. Jette, M. Dasso, A. Patke, A.F. Palazzo, A.A. Kossiakoff, and A. Hoelz. 2022. Architecture of the cytoplasmic face of the nuclear pore. *Science*. 376:eabm9129. doi:10.1126/science.abm9129.

Carlon-Andres, I., F. Lagadec, N. Pied, F. Rayne, M.-E. Lafon, R.H. Kehlenbach, and H. Wodrich. 2020. Nup358 and Transportin 1 Cooperate in Adenoviral Genome Import. *J. Virol.* 94:e00164-20. doi:10.1128/JVI.00164-20.

Carter, T., and M. Iqbal. 2024. The Influenza A Virus Replication Cycle: A Comprehensive Review. *Viruses*. 16:316. doi:10.3390/v16020316.

Chatur, N., C. Yea, B. Ertl-Wagner, and E.A. Yeh. 2022. Outcomes in influenza and *RANBP2* mutation-associated acute necrotizing encephalopathy of childhood. *Dev. Med. Child Neurol.* 64:1008–1016. doi:10.1111/dmcn.15165.

Clohisey, S., and J.K. Baillie. 2019. Host susceptibility to severe influenza A virus infection. *Crit. Care*. 23:303. doi:10.1186/s13054-019-2566-7.

Copeland, A.M., W.W. Newcomb, and J.C. Brown. 2009. Herpes Simplex Virus Replication: Roles of Viral Proteins and Nucleoporins in Capsid-Nucleus Attachment. *J. Virol.* 83:1660–1668. doi:10.1128/JVI.01139-08.

Cros, J.F., A. García-Sastre, and P. Palese. 2005. An Unconventional NLS is Critical for the Nuclear Import of the Influenza A Virus Nucleoprotein and Ribonucleoprotein. *Traffic*. 6:205–213. doi:10.1111/j.1600-0854.2005.00263.x.

Desgraupes, S., L. Etienne, and N.J. Arhel. 2023. RANBP2 evolution and human disease. *FEBS Lett.* 597:2519–2533. doi:10.1002/1873-3468.14749.

Di Nunzio, F., A. Danckaert, T. Fricke, P. Perez, J. Fernandez, E. Perret, P. Roux, S. Shorte, P. Charneau, F. Diaz-Griffero, and N.J. Arhel. 2012. Human Nucleoporins Promote HIV-1

Docking at the Nuclear Pore, Nuclear Import and Integration. *PLoS ONE*. 7:e46037. doi:10.1371/journal.pone.0046037.

Dou, D., R. Revol, H. Östbye, H. Wang, and R. Daniels. 2018. Influenza A Virus Cell Entry, Replication, Virion Assembly and Movement. *Front. Immunol.* 9:1581. doi:10.3389/fimmu.2018.01581.

Elton, D., M. Simpson-Holley, K. Archer, L. Medcalf, R. Hallam, J. McCauley, and P. Digard. 2001. Interaction of the Influenza Virus Nucleoprotein with the Cellular CRM1-Mediated Nuclear Export Pathway. *J. Virol.* 75:408–419. doi:10.1128/JVI.75.1.408-419.2001.

Fernandez, J., C. Hassen-Khodja, V. Georget, T. Rose, Y. Jacob, Y.L. Janin, S. Nisole, P.-O. Vidalain, and N.J. Arhel. 2021. Measuring the subcellular compartmentalization of viral infections by protein complementation assay. *Proc. Natl. Acad. Sci.* 118:e2010524118. doi:10.1073/pnas.2010524118.

Fodor, E., and A.J.W. Te Velthuis. 2020. Structure and Function of the Influenza Virus Transcription and Replication Machinery. *Cold Spring Harb. Perspect. Med.* 10:a038398. doi:10.1101/cshperspect.a038398.

Gounder, A.P., and A.C.M. Boon. 2019. Influenza Pathogenesis: The Effect of Host Factors on Severity of Disease. *J. Immunol. Baltim. Md 1950*. 202:341–350. doi:10.4049/jimmunol.1801010.

Gouy, B., A. Decorsière, S. Desgraupes, W. Duan, H. Ouyang, Y.E. Wang, E.A. Yeh, A.F. Palazzo, T.J. Moraes, S. Nisole, and N.J. Arhel. 2023. Rapid and inexpensive bedside diagnosis of RAN binding protein 2-associated acute necrotizing encephalopathy. *Front. Neurol.* 14:1282059. doi:10.3389/fneur.2023.1282059.

Hemerka, J.N., D. Wang, Y. Weng, W. Lu, R.S. Kaushik, J. Jin, A.F. Harmon, and F. Li. 2009. Detection and Characterization of Influenza A Virus PA-PB2 Interaction through a Bimolecular Fluorescence Complementation Assay. *J. Virol.* 83:3944–3955. doi:10.1128/JVI.02300-08.

Hofemeister, H., and P. O'Hare. 2008. Nuclear pore composition and gating in herpes simplex virus-infected cells. *J. Virol.* 82:8392–8399. doi:10.1128/JVI.00951-08.

Huet, S., S.V. Avilov, L. Ferbitz, N. Daigle, S. Cusack, and J. Ellenberg. 2010. Nuclear Import and Assembly of Influenza A Virus RNA Polymerase Studied in Live Cells by Fluorescence Cross-Correlation Spectroscopy. *J. Virol.* 84:1254–1264. doi:10.1128/JVI.01533-09.

Hutten, S., A. Flotho, F. Melchior, and R.H. Kehlenbach. 2008. The Nup358-RanGAP Complex Is Required for Efficient Importin α/β-dependent Nuclear Import. *Mol. Biol. Cell*. 19:2300–2310. doi:10.1091/mbc.e07-12-1279.

543 Iwasaki, A., and P.S. Pillai. 2014. Innate immunity to influenza virus infection. *Nat. Rev. Immunol.*
544 14:315–328. doi:10.1038/nri3665.

545 Jiang, J., Y.E. Wang, A.F. Palazzo, and Q. Shen. 2022. Roles of Nucleoporin RanBP2/Nup358 in
546 Acute Necrotizing Encephalopathy Type 1 (ANE1) and Viral Infection. *Int. J. Mol. Sci.*
547 23:3548. doi:10.3390/ijms23073548.

548 Joseph, J., and M. Dasso. 2008. The nucleoporin Nup358 associates with and regulates
549 interphase microtubules. *FEBS Lett.* 582:190–196. doi:10.1016/j.febslet.2007.11.087.

550 Khanna, M., K. Sharma, S.K. Saxena, J.G. Sharma, R. Rajput, and B. Kumar. 2024. Unravelling the
551 interaction between Influenza virus and the nuclear pore complex: insights into viral
552 replication and host immune response. *VirusDisease*. 35:231–242. doi:10.1007/s13337-
553 024-00879-6.

554 Koh, J.C., A. Murugasu, J. Krishnappa, and T. Thomas. 2019. Favorable Outcomes With Early
555 Interleukin 6 Receptor Blockade in Severe Acute Necrotizing Encephalopathy of
556 Childhood. *Pediatr. Neurol.* 98:80–84. doi:10.1016/j.pediatrneurol.2019.04.009.

557 Lee, V.W.M., T.B. Khoo, C.M. Teh, H.S. Heng, L. Li, Y.L.M. Yusof, N.A. Yahaya, S. Dharshini, S.W.
558 Wong, T. Nickson, and ANE Malaysia Outcome Study Group. 2023. Factors associated
559 with outcomes of severe acute necrotizing encephalopathy: A multicentre experience in
560 Malaysia. *Dev. Med. Child Neurol.* 65:1256–1263. doi:10.1111/dmcn.15536.

561 Levine, J.M., N. Ahsan, E. Ho, and J.D. Santoro. 2020. Genetic Acute Necrotizing Encephalopathy
562 Associated with RANBP2: Clinical and Therapeutic Implications in Pediatrics. *Mult. Scler.*
563 *Relat. Disord.* 43:102194. doi:10.1016/j.msard.2020.102194.

564 Li, J., L. Su, J. Jiang, Y.E. Wang, Y. Ling, Y. Qiu, H. Yu, Y. Huang, J. Wu, S. Jiang, T. Zhang, A.F.
565 Palazzo, and Q. Shen. 2023. RanBP2/Nup358 Mediates Sumoylation of STAT1 and
566 Antagonizes Interferon-α-Mediated Antiviral Innate Immunity. *Int. J. Mol. Sci.* 25:299.
567 doi:10.3390/ijms25010299.

568 Ma, K., A.-M.M. Roy, and G.R. Whittaker. 2001. Nuclear Export of Influenza Virus
569 Ribonucleoproteins: Identification of an Export Intermediate at the Nuclear Periphery.
570 *Virology*. 282:215–220. doi:10.1006/viro.2001.0833.

571 Maarifi, G., J. Fernandez, D.M. Portilho, A. Boulay, J. Dutrieux, S. Oddos, G. Butler-Browne, S.
572 Nisole, and N.J. Arhel. 2018. RanBP2 regulates the anti-retroviral activity of TRIM5α by
573 SUMOylation at a predicted phosphorylated SUMOylation motif. *Commun. Biol.* 1:193.
574 doi:10.1038/s42003-018-0198-0.

575 Mettelman, R.C., and P.G. Thomas. 2021. Human Susceptibility to Influenza Infection and Severe
576 Disease. *Cold Spring Harb. Perspect. Med.* 11:a038711.
577 doi:10.1101/cshperspect.a038711.

Miyake, Y., J.J. Keusch, L. Decamps, H. Ho-Xuan, S. Iketani, H. Gut, U. Kutay, A. Helenius, and Y. Yamauchi. 2019. Influenza virus uses transportin 1 for vRNP debundling during cell entry. *Nat. Microbiol.* 4:578–586. doi:10.1038/s41564-018-0332-2.

Mizuguchi, M., H. Yamanouchi, T. Ichiyama, and M. Shiomi. 2007. Acute encephalopathy associated with influenza and other viral infections. *Acta Neurol. Scand.* 115:45–56. doi:10.1111/j.1600-0404.2007.00809.x.

Munier, S., T. Rolland, C. Diot, Y. Jacob, and N. Naffakh. 2013. Exploration of Binary Virus–Host Interactions Using an Infectious Protein Complementation Assay. *Mol. Cell. Proteomics*. 12:2845–2855. doi:10.1074/mcp.M113.028688.

Neilson, D.E., R.M. Eiben, S. Waniewski, C.L. Hoppel, M.E. Varnes, B.A. Bangert, M. Wiznitzer, M.L. Warman, and D.S. Kerr. 2003. Autosomal dominant acute necrotizing encephalopathy. *Neurology*. 61:226–230. doi:10.1212/01.WNL.0000073544.28775.1A.

Nguyen, N.L.T., W. Wu, and N. Panté. 2023. Contribution of the Nuclear Localization Sequences of Influenza A Nucleoprotein to the Nuclear Import of the Influenza Genome in Infected Cells. *Viruses*. 15:1641. doi:10.3390/v15081641.

Okumura, A., M. Mizuguchi, H. Kidokoro, M. Tanaka, S. Abe, M. Hosoya, H. Aiba, Y. Maegaki, H. Yamamoto, T. Tanabe, E. Noda, G. Imataka, and H. Kurahashi. 2009. Outcome of acute necrotizing encephalopathy in relation to treatment with corticosteroids and gammaglobulin. *Brain Dev.* 31:221–227. doi:10.1016/j.braindev.2008.03.005.

Portilho, D.M., J. Fernandez, M. Ringeard, A.K. Machado, A. Boulay, M. Mayer, M. Müller-Trutwin, A.-S. Beignon, F. Kirchhoff, S. Nisole, and N.J. Arhel. 2016. Endogenous TRIM5α Function Is Regulated by SUMOylation and Nuclear Sequestration for Efficient Innate Sensing in Dendritic Cells. *Cell Rep.* 14:355–369. doi:10.1016/j.celrep.2015.12.039.

Sakuma, H., T. Thomas, C. Debinski, M. Eyre, V.X. Han, H.F. Jones, G. Kawano, V.W. Lee, S. Malone, T. Matsuishi, S.S. Mohammad, T. Mori, H. Nishida, M. Nosadini, J.-I. Takanashi, M. Mizuguchi, M. Lim, and R.C. Dale. 2025. International consensus definitions for infection-triggered encephalopathy syndromes. *Dev. Med. Child Neurol.* 67:195–207. doi:10.1111/dmcn.16067.

Schaller, T., K.E. Ocwieja, J. Rasaiyaah, A.J. Price, T.L. Brady, S.L. Roth, S. Hué, A.J. Fletcher, K. Lee, V.N. KewalRamani, M. Noursadeghi, R.G. Jenner, L.C. James, F.D. Bushman, and G.J. Towers. 2011. HIV-1 Capsid-Cyclophilin Interactions Determine Nuclear Import Pathway, Integration Targeting and Replication Efficiency. *PLOS Pathog.* 7:e1002439. doi:10.1371/journal.ppat.1002439.

Shen, Q., Y.E. Wang, M. Truong, K. Mahadevan, J.J. Wu, H. Zhang, J. Li, H.W. Smith, C.A. Smibert, and A.F. Palazzo. 2021. RanBP2/Nup358 enhances miRNA activity by sumoylating Argonautes. *PLOS Genet.* 17:e1009378. doi:10.1371/journal.pgen.1009378.

Sugaya, N. 2002. Influenza-associated encephalopathy in Japan. *Semin. Pediatr. Infect. Dis.* 13:79–84. doi:10.1053/spid.2002.122993.

Watanabe, K., N. Takizawa, M. Katoh, K. Hoshida, N. Kobayashi, and K. Nagata. 2001. Inhibition of nuclear export of ribonucleoprotein complexes of influenza virus by leptomycin B. *Virus Res.* 77:31–42. doi:10.1016/S0168-1702(01)00263-5.

Watanabe, T., S. Watanabe, and Y. Kawaoka. 2010. Cellular Networks Involved in the Influenza Virus Life Cycle. *Cell Host Microbe*. 7:427–439. doi:10.1016/j.chom.2010.05.008.

Wu, J., M.J. Matunis, D. Kraemer, G. Blobel, and E. Coutavas. 1995. Nup358, a Cytoplasmically Exposed Nucleoporin with Peptide Repeats, Ran-GTP Binding Sites, Zinc Fingers, a Cyclophilin A Homologous Domain, and a Leucine-rich Region. *J. Biol. Chem.* 270:14209–14213. doi:10.1074/jbc.270.23.14209.

Wu, X., W. Wu, W. Pan, L. Wu, K. Liu, and H.-L. Zhang. 2015. Acute Necrotizing Encephalopathy: An Underrecognized Clinicoradiologic Disorder. *Mediators Inflamm.* 2015:792578. doi:10.1155/2015/792578.

Yokoyama, N., N. Hayashi, T. Seki, N. Panté, T. Ohba, K. Nishii, K. Kuma, T. Hayashida, T. Miyata, U. Aebi, M. Fukui, and T. Nishimoto. 1995. A giant nucleopore protein that binds Ran/TC4. *Nature*. 376:184–188. doi:10.1038/376184a0.

Zhang, R., R. Mehla, and A. Chauhan. 2010. Perturbation of Host Nuclear Membrane Component RanBP2 Impairs the Nuclear Import of Human Immunodeficiency Virus -1 Preintegration Complex (DNA). *PLoS ONE*. 5:e15620. doi:10.1371/journal.pone.0015620.

Zhu, Z., E. Fodor, and J.R. Keown. 2023. A structural understanding of influenza virus genome replication. *Trends Microbiol.* 31:308–319. doi:10.1016/j.tim.2022.09.015.

638 **FIGURE LEGENDS**

639 **Figure 1: Knockdown of RANBP2 stimulates non-productive Influenza vRNA replication in infected cells**
640 **without altering the initial vRNP import into the nucleus.**

641 **(A)** A549 cells were transduced with LV shRNA-Control or shRANBP2, and infected with influenza A virus
642 (IAV) (A/WSN/1933) at MOI 0.5. RANBP2 transcripts were quantified by RT-qPCR and normalized on
643 RPL13a housekeeping gene and on the control condition. Supernatants were harvested at 10h post-
644 infection and viral titers were determined by TCID50 assay on MDCK cells. Results represent mean values
645 +/- SD. **(B)** A549 cells or **(C)** THP-1 cells were transduced with LV shRNA-Control or -RANBP2 or not
646 transduced (NTD) then infected with influenza A virus (A/WSN/1933) at MOI 0.5. At the indicated time
647 points, cells were lysed and total intracellular RNAs were extracted. Viral RNAs encoding the Matrix 1
648 (M1) protein were amplified by RTqPCR. **(D)** Nucleoprotein-encoding (NP) viral RNAs were amplified by
649 RTqPCR in the A549 infected cells. Results from B-C-D are normalized on a housekeeping gene and on
650 the control condition. Results are presented as mean +/- SD. **(E)** Housekeeping gene expression was not
651 affected by the knock down. **(F)** Transduced A549 cells were infected at MOI 0.5 and total intracellular
652 RNAs were extracted at 6h post-infection. Strand-specific reverse transcription (RT) was performed with
653 tagged-primers to amplify separately the genomic viral RNA (vRNA) and the complementary viral RNA
654 (cRNA). M1-encoding viral RNAs were amplified by RTqPCR. Results are normalized on the control
655 condition and presented as mean +/- SD. **(G)** Transduced A549 cells were infected at MOI 0.5 and stained
656 for the NP at 8h post-infection. Scale bar: 20µm. **(H)** Cytoplasmic fluorescence was quantified using the
657 Fiji software. Each dot represents the cytoplasmic fluorescence of a cell, normalized by its area. **(I)**
658 Transduced A549 cells were infected at MOI 0.5 and co-stained for the NP and PB1 proteins at 8h post-
659 infection. Scale bar: 20µm. B**J)** Colocalization was quantified using the Fiji software. **(K)** Transduced A549
660 cells were infected at MOI 4 and stained for the NP at 1h post-infection. Scale bar: 20µm. **(L)** Confocal
661 Airyscan image processing and quantifications were performed in the Fiji software. Each dot represents
662 the cytoplasmic fluorescence of a cell, normalized by its area. **(M)** Transduced A549 cells were infected
663 at MOI 4 and stained for the NP at 2h post-infection. Scale bar: 20µm. **(N)** Nuclear fluorescence was
664 quantified using the Fiji software. Each dot represents the nuclear fluorescence of a cell. **(O)**
665 Experimental strategy of the Alpha-Centauri assay. IAV (A/WSN/1933) particles containing the PB2
666 protein fused to a fragment of the NanoLuc (α-Nluc) were produced by reverse genetics. A plasmid
667 containing a nuclear localization signal (NLS) fused to the other fragment of the NanoLuc (Centauri-Nluc)
668 was generated and transfected into A549 cells. Transfected cells were infected at MOI 4 and the
669 luminescence was measured to assess the NanoLuc complementation upon nuclear import of the viral
670 ribonucleoproteins. **(P)** NanoLuc complementation results are normalized on the last time point. Two-
671 tailed unpaired Student's t test. *P < 0.05, **P < 0.002, ***P < 0.0002, ****P < 0.0001, ns: non-
672 significant.

673 **Figure 2: RANBP2 Knockdown facilitates the Nuclear Reimport of the viral polymerase complex**
674 **proteins PB1/PB2/PA and segment-selective vRNP over-export to the cytoplasm.**

675 **(A)** A549 cells were transduced with LV shRNA-Control or shRNA-RANBP2 and infected with influenza A
676 virus (IAV) (A/WSN/1933) at MOI 4. At 6h post-infection, protein levels of PB1, PB2, PA and NP were
677 determined by western blot. **(B)** Transduced A549 cells were treated with KPT-330 for 2h and infected
678 with IAV at MOI 0.5. Nucleo-cytoplasmic fractionation was performed at 6h post-infection and PB1, PB2
679 and PA levels were determined by western blot (N: nucleus, C: cytoplasm). Lamin and tubulin protein
680 levels were investigated to verify the efficacy of the fractionation. **(C)** Transduced A549 cells were
681 infected with IAV at MOI 0.5 in the absence of KPT-330. The PB1 was stained at 6h post-infection and
682 nuclear fluorescence **(Figure S7)** was quantified using the Fiji software. Each dot represents the nuclear
683 fluorescence of a cell. **(D)** Strand- and segment-specific RTqPCR strategy. Strand-specific reverse

684 transcription (RT) was performed with tagged-primers to amplify separately the genomic viral RNA
685 (vRNA) and the complementary viral RNA (cRNA). Each of the 8 segments of IAV were then amplified by
686 qPCR using specific primers. **(E)** Transduced A549 cells were infected with IAV at MOI 0.5. At 6h post-
687 infection, nuclear (N) and cytoplasmic (C) fractions were separated and total intracellular RNAs were
688 extracted. cRNAs were reverse transcribed by strand-specific RTqPCR and results were normalized on the
689 nuclear fraction of the control condition. **(F)** vRNAs were reverse transcribed by strand-specific RTqPCR
690 and results were normalized on the control condition of each fraction. Results are presented as mean +/-
691 SD.

692 **Figure 3: RANBP2 knockdown exacerbates the inflammatory response to IAV infection.**

693 **(A)** Monocyte-derived macrophages (MDM), THP-1 cells and A549 cells were transduced with LV shRNA-
694 Control or shRNA-RANBP2 at MOI 30 and stimulated with influenza A virus (IAV) (A/WSN/1933) at MOI
695 0.1 overnight. Cytokine transcripts were assessed by RT-qPCR and results were normalized on RPL13a or
696 β-actin and on the non-stimulated control condition. Results are presented as mean +/- SD. Two-tailed
697 unpaired Student's t test. *P < 0.05, **P < 0.002, ***P < 0.0002, ****P < 0.0001, ns: non-significant. **(B)**
698 Supernatants from IAV-stimulated MDM were collected at 24h post-stimulation and pro-inflammatory
699 mediators were quantified by multiplex LUMINEX assay on samples diluted 1:50. The mean fluorescence
700 intensities (MFI) for RANBP2-KD samples were normalized on the Control samples. Results are
701 represented as heat maps of fold values.

702 **Figure 4: Mislocalisation of the ANE1-mutated N-terminal part of RANBP2 drives hyper-inflammation**
703 **upon immune stimulation.**

704 **(A)** CRISPR editing strategy. A guide sgRNA hybridizing directly upstream the C1754 position was used to
705 induce the cleavage by the Cas9 enzyme. A donor DNA sequence carrying the C1754T mutation
706 (corresponding to T585M at the protein level) was supplied. After homology directed repair (HDR), three
707 types of CRISPR clones were generated (box below): (top) WT homozygous clones (middle) WT/C1754T
708 heterozygous clones and (bottom) C1754T/C1754T homozygous clones. **(B)** RNA expression of the WT or
709 C1754T form of RANBP2 was assessed by RANBP2-specific RTqPCR. HEK-293T cells transfected with
710 plasmids encoding the WT form, the T585M form or both forms of RANBP2 were used as control. **(C)**
711 Illustration of the RANBP2 sequence from positions 1749 to 1757, carrying a C on the WT sequence at
712 position 1754, replaced by a T on the T585M mutant. **(D)** Sanger sequencing of the CRISPR clones
713 showing either a C, a T or both at position 1754. **(E)** CRISPR clones were stimulated overnight either by
714 IAV (A/WSN/1933) at MOI 0.5 or by transfection with the 2CARD module of RIG-I, and total intracellular
715 RNAs were extracted. Pro-inflammatory cytokine expression was assessed by RTqPCR to detect CXCL10
716 and TNFα transcripts. Values were normalized on RPL13a and for the untransfected control condition.
717 Results are presented as mean +/- SD. **(F)** CRISPR clones were fixed and stained for RANBP2 using either
718 an antibody recognizing the NTD (amino acids 1 to 18) or the CTD (amino acids 2550 to 2837) parts of
719 RANBP2. **(G)** Schematic representation of the RANBP2 protein sequence and the epitopes recognized by
720 the antibodies. Nuclear fluorescence was quantified using the Fiji software for **(H)** $RANBP2^{NTD}$ and **(I)**
721 $RANBP2^{CTD}$.

722 **SUPPLEMENTARY FIGURE LEGENDS**

723 **Figure S1: Assessment of RANBP2 knock-down in human primary macrophages and A549 cells.**

724 **(A)** Monocyte-derived macrophages (MDM) were transduced with LV shRNA-Control or shRNA-RANBP2
725 at MOI 20. Knock-down efficacy was assessed by RTqPCR at 24h post-infection **(B)** Knock-down efficacy
726 was confirmed by Western blot in A549 cells at 72h post-infection.

727 **Figure S2: RT-qPCR strategy to distinguish cRNA and vRNA.**

(A) Strand-specific Reverse Transcription (RT) strategy. Genomic viral RNAs (vRNA) and complementary RNAs (cRNA) were reverse transcribed using specific tagged-primers hybridizing to the consensus 3'-sequences of each of the 8 viral segments. **(B)** Validation of the specificity of the strand-specific RT. qPCR primers complementary to the tags were used to amplify cDNAs produced by each RT and verify that only vRNAs were amplified after vRNA-specific RT, only cRNAs after cRNA-specific RT and no cellular RNAs were reverse transcribed by any of the two RT. RT-specificity was check for 2 segments (segment 1 and segment 4).

Figure S3: Increase in cytoplasmic NP in RANBP2-KD cells at 8 hpi.

Full panel of images for Figure 1G. A549 cells were transduced or not (NTD) with LV shRNA-Control or shRNA-RANBP2 and infected with influenza A virus (IAV) (A/WSN/1933) at MOI 0.5. At 8h post-infection, cells were fixed and stained for the nucleoprotein (NP). Scale bar: 20µm. Image processing was done using the Fiji software. NP (AlexaFluor-488) and shRNA (mCherry) colors were changed to « Orange Hot » and « cyan » for aesthetic purposes.

Figure S4: Increase in cytoplasmic vRNP in RANBP2-KD cells at 8 hpi.

Transduced A549 cells were infected at MOI 0.5 and co-stained for the NP and PA proteins at 8h post-infection. Scale bar: 20µm. Colocalization was quantified using the Fiji software.

Figure S5: Alpha-Centauri assay to measure IAV nuclear import.

(A-B) A549 cells were transduced with a plasmid containing the Centauri-Nluc tagged with HA. Cells were stained for the HA and analyzed by flow cytometry to determine the percentage of transduced cells. **(C)** Cells were infected at MOI 4 and the luminescence was measured to assess the Nanoluciferase complementation upon nuclear import of the viral ribonucleoproteins. **(D)** Centauri-Nluc-transduced A549 cells were transduced with LV shRNA-Control or shRNA-RANBP2 expressing the mCherry. The percentage of mCherry-positive cells was determined by flow cytometry.

Figure S6: Inhibition of CRM1-dependent NP export using KPT-330/Selinexor.

A549 cells were treated or not (Vehicle) with KPT-330 at the indicated doses for 2 h at 37°C, then infected with IAV. **(A)** Cells were fixed and stained for the NP at 8 hour post-infection (hpi) to verify the efficacy of the NP export inhibition. **(B)** KPT-330 cytotoxicity was assessed by MTT assay. Uninfected cells were incubated with MTT (5 mg/mL) for 3 h at 37°C. Acid isopropanol was added and absorbance was read at 570nm. **(C)** At the indicated times post-infection, cells were fixed and stained for the NP to determine when vRNP export starts.

Figure S7: Increase in nuclear PB1 in RANBP2-KD cells.

Full panel of images for Figure 2D. A549 cells were transduced with LV shRNA-Control or shRNA-RANBP2 and infected with influenza A virus (IAV) (A/WSN/1933) at MOI 0.5. At 6h post-infection, cells were fixed and the PB1 protein was stained. Scale bar: 20µm. Image processing was done using the Fiji software.

Figure S8: qPCR strategy to amplify the 8 segments of IAV.

(A) Segment-specific qPCR strategy. After strand-specific RT, the 8 segments were detected using qPCR primers amplifying the indicated regions of each segments. All 8 segments were amplified after each RT. **(B)** Segment-specific qPCR was performed after total RT (amplifying all RNAs) and all primer pairs were still specific of the viral RNA segments. Melting curves are presented.

Figure S9: Phenotypic analysis of primary human MDM.

PBMCs were isolated from blood samples of two healthy donors. Monocytes were isolated by plastic adherence for 45 minutes and differentiated into macrophages by addition of GM-CSF. After 7 days of

differentiation, monocyte-derived macrophages from 2 donors were stained for phenotypic markers. The expression of CD3, CD14, CD16, CD11b, HLA-DR and CD80 was assessed by flow cytometry.

Figure S10: Stimulation of MDM with IAV triggers IL-6 and IL-1β synthesis.

PBMCs were isolated from blood samples of two healthy donors. Monocytes were isolated by plastic adherence for 45 minutes. Supernatants containing the peripheral blood lymphocytes (PBL) were collected. Macrophages were differentiated by addition of GM-CSF to monocytes for 7 days at 37°C. Each cell types was infected with influenza A virus (IAV) (A/WSN/1933) at MOI 0.5. At 16h post-infection, total intracellular RNAs were extracted. **(A)** M1-encoding viral RNAs were amplified by RTqPCR. (**B)** IL-6 and IL-1ß RNAs were amplified by RTqPCR. Results are presented as mean +/- SD and normalized on the non-infected condition for each cell type.

Figure S11: CRISPR-Cas9 knock-in strategy to generate ANE1-variants in U2OS cells.

(A) RANBP2-specific allelic qPCR strategy. RANBP2-specific reverse transcription was performed using a primer specific to the RANBP2 sequence and not present on the highly homologous RGPD sequence (conserved parts are indicated in gray). Mutant and WT RANBP2 were distinguished using a reverse qPCR primer carrying either an A or a G at its 3' end. A set of primers was also designed to amplify RANBP2 (near the same region) without distinguishing both forms. **(B)** Representation of the RANBP2 sequence upstream of the repair site, and one of the eight RGPDs. Sanger sequencing of the CRISPR clones shows no recombination with the RGPD sequence as all carry a G at the indicated positions (black arrows). **(C)** To produce controls for the screening of CRISPR clones by allelic qPCR, HEK-293T cells were transfected with mCherry-shRNA-RANBP2 and either GFP-RANBP2-WT, GFP-RANBP2-T585M or both. mCherry-expressing cells were sorted by FACS and total intracellular RNAs were extracted for the allelic RTqPCR. Results of the FACS sorting are presented.

Figure S12: Localization of RANBP2 in CRISPR knock-in clones

CRISPR knock-in clones were fixed and stained for RANBP2 (Proteintech 27606-1-AP) and FG-repeats (Biolegend mab414) to investigate the localization of RANBP2. **(A)** Full sets of confocal images used for the quantification of RANBP2 at the nuclear rim. Scale bar = 5µm. **(B)** Higher resolution images obtained by confocal microscopy. Scale bar = 5µm.

SUPPLEMENTARY TABLE LEGENDS

Table S1: List of plasmids.

Table S2: List of reverse transcription and qPCR primers.

Table S3: List of antibodies.

Figure 1

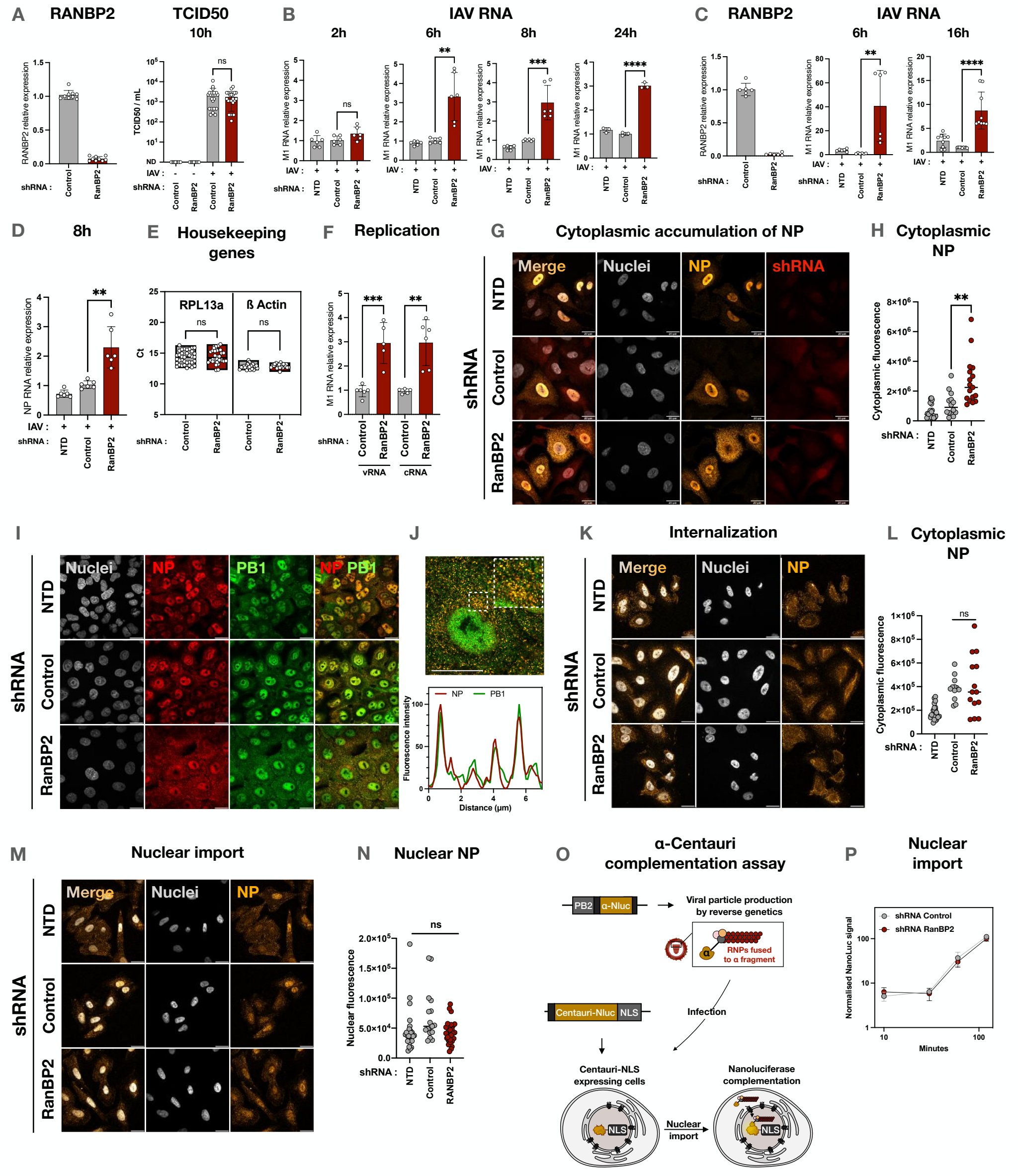
A
RANBP2
TCID50
10h
B
IAV RNA
2h
6h
8h
24h
C
RANBP2
IAV RNA
6h
16h
D
8h
E
Housekeeping genes
RPL13a
ß Actin
F
Replication
vRNA
cRNA
G
Cytoplasmic accumulation of NP
Merge
Nuclei
NP
shRNA
NTD
Control
RanBP2
H
Cytoplasmic NP
I
PB1
NP PB1
Fluorescence intensity
Distance (µm)
J
K
Internalization
L
Cytoplasmic NP
M
Nuclear import
N
Nuclear NP
O
α-Centauri complementation assay
PB2
α-Nluc
Viral particle production by reverse genetics
RNPs fused to α fragment
Centauri-Nluc
NLS
Infection
Centauri-NLS expressing cells
Nanoluciferase complementation
Nuclear import
P
Nuclear import
shRNA Control
shRNA RanBP2
Normalised NanoLuc signal
Minutes

Figure 2

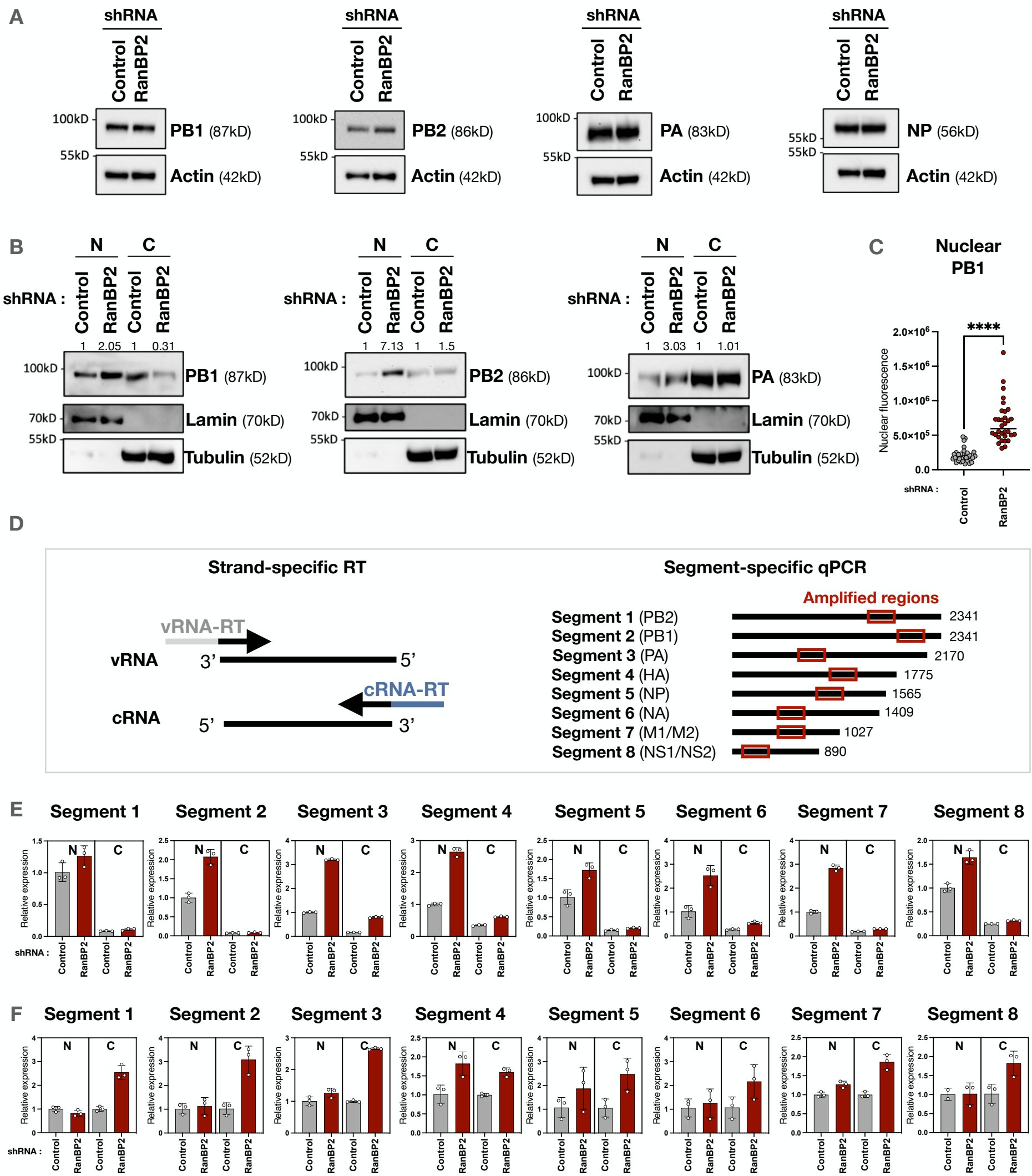
A
shRNA
Control
RanBP2
100kD
55kD
PB1 (87kD)
Actin (42kD)
PB2 (86kD)
PA (83kD)
NP (56kD)
B
N
C
shRNA :
1 2.05 1 0.31
1 7.13 1 1.5
1 3.03 1 1.01
Lamin (70kD)
Tubulin (52kD)
70kD
C
Nuclear PB1
****
Nuclear fluorescence
2.0×10^6
1.5×10^6
1.0×10^6
5.0×10^5
0.0
D
Strand-specific RT
vRNA-RT
vRNA
3'
5'
cRNA-RT
cRNA
Segment-specific qPCR
Amplified regions
Segment 1 (PB2) 2341
Segment 2 (PB1) 2341
Segment 3 (PA) 2170
Segment 4 (HA) 1775
Segment 5 (NP) 1565
Segment 6 (NA) 1409
Segment 7 (M1/M2) 1027
Segment 8 (NS1/NS2) 890
E
Segment 1
Segment 2
Segment 3
Segment 4
Segment 5
Segment 6
Segment 7
Segment 8
Relative expression
F

Figure 3

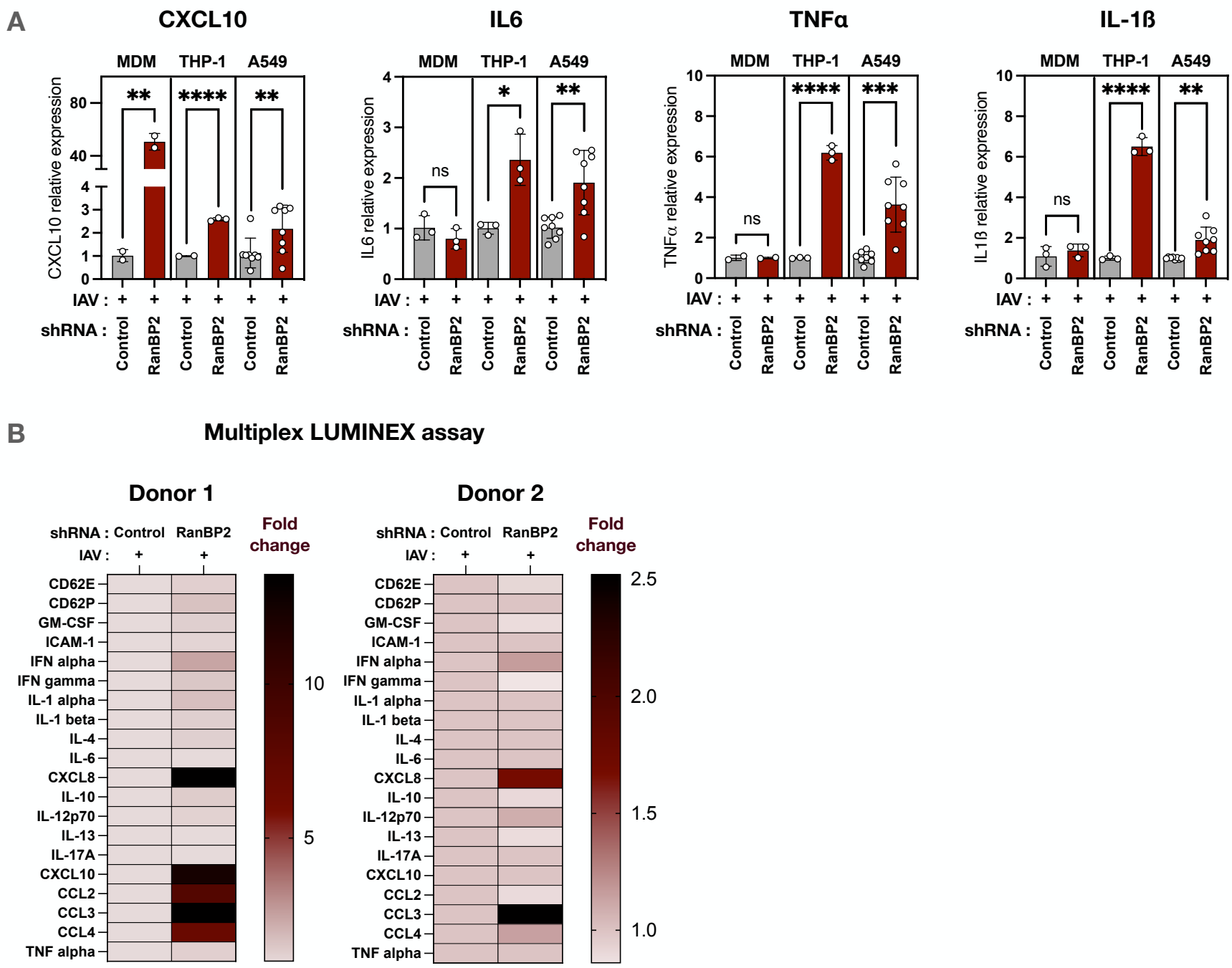
A
CXCL10
IL6
TNFα
IL-1ß
MDM
THP-1
A549
CXCL10 relative expression
IL6 relative expression
TNFα relative expression
IL1ß relative expression
ns
IAV :
shRNA :
Control
RanBP2
B
Multiplex LUMINEX assay
Donor 1
Donor 2
shRNA : Control RanBP2
IAV :
Fold change
CD62E
CD62P
GM-CSF
ICAM-1
IFN alpha
IFN gamma
IL-1 alpha
IL-1 beta
IL-4
IL-6
CXCL8
IL-10
IL-12p70
IL-13
IL-17A
CXCL10
CCL2
CCL3
CCL4
TNF alpha

Figure 4

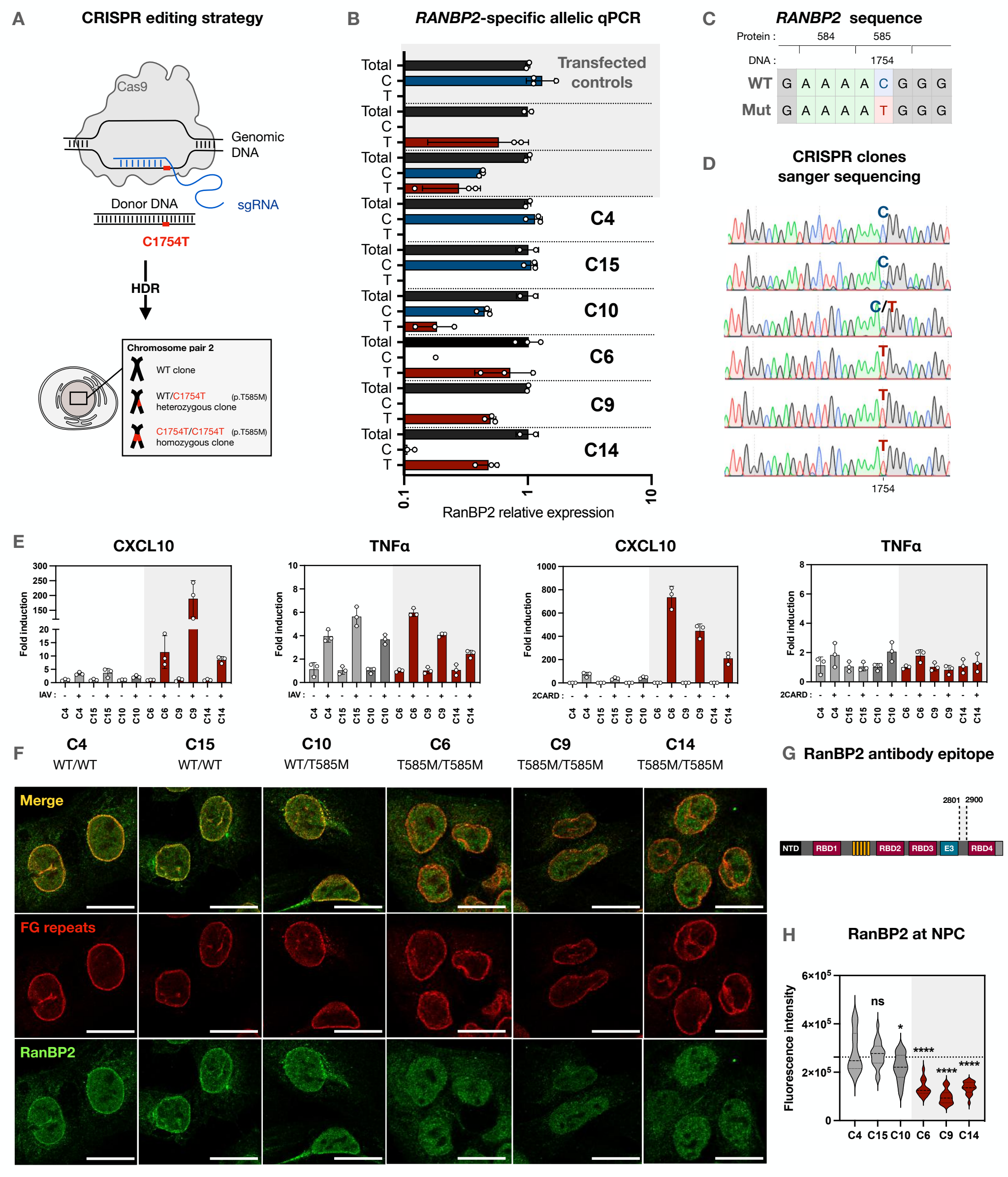
A
CRISPR editing strategy
Cas9
Genomic DNA
Donor DNA
sgRNA
C1754T
HDR
Chromosome pair 2
WT clone
WT/C1754T (p.T585M) heterozygous clone
C1754T/C1754T (p.T585M) homozygous clone
B
RANBP2-specific allelic qPCR
Transfected controls
Total
C
T
C4
C15
C10
C6
C9
C14
0.1
1
10
RanBP2 relative expression
C
RANBP2 sequence
Protein :
584
585
DNA :
1754
WT G A A A A C G G G
Mut G A A A A T G G G
D
CRISPR clones sanger sequencing
C
C
C/T
T
T
T
1754
E
CXCL10
TNFα
CXCL10
TNFα
Fold induction
IAV :
2CARD :
C4 C4 C15 C15 C10 C10 C6 C6 C9 C9 C14 C14
F
C4 WT/WT
C15 WT/WT
C10 WT/T585M
C6 T585M/T585M
C9 T585M/T585M
C14 T585M/T585M
Merge
FG repeats
RanBP2
G
RanBP2 antibody epitope
2801
2900
NTD
RBD1
RBD2
RBD3
E3
RBD4
H
RanBP2 at NPC
Fluorescence intensity
ns
*
****
****
****
C4 C15 C10 C6 C9 C14

Supplementary

Supplemental Figure S1

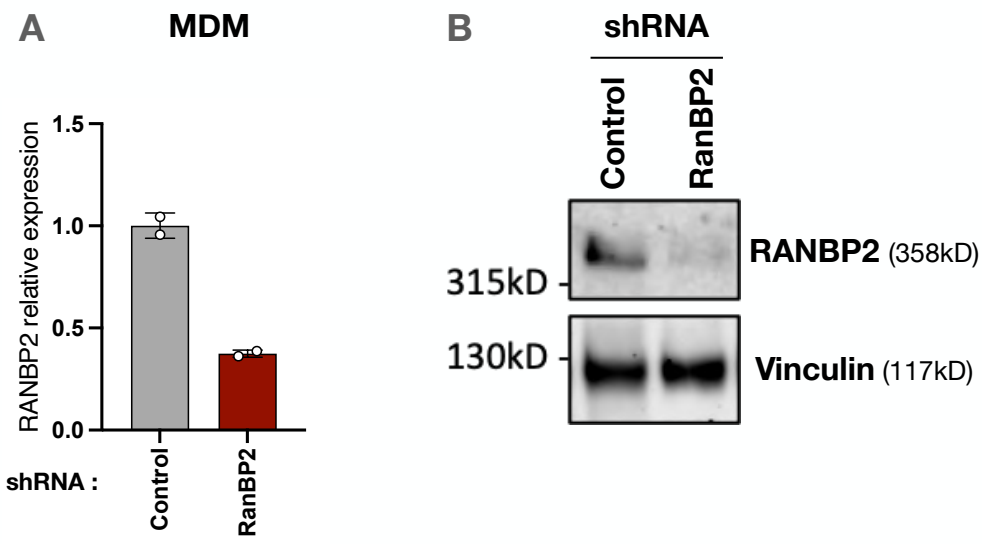

Supplemental Figure S2

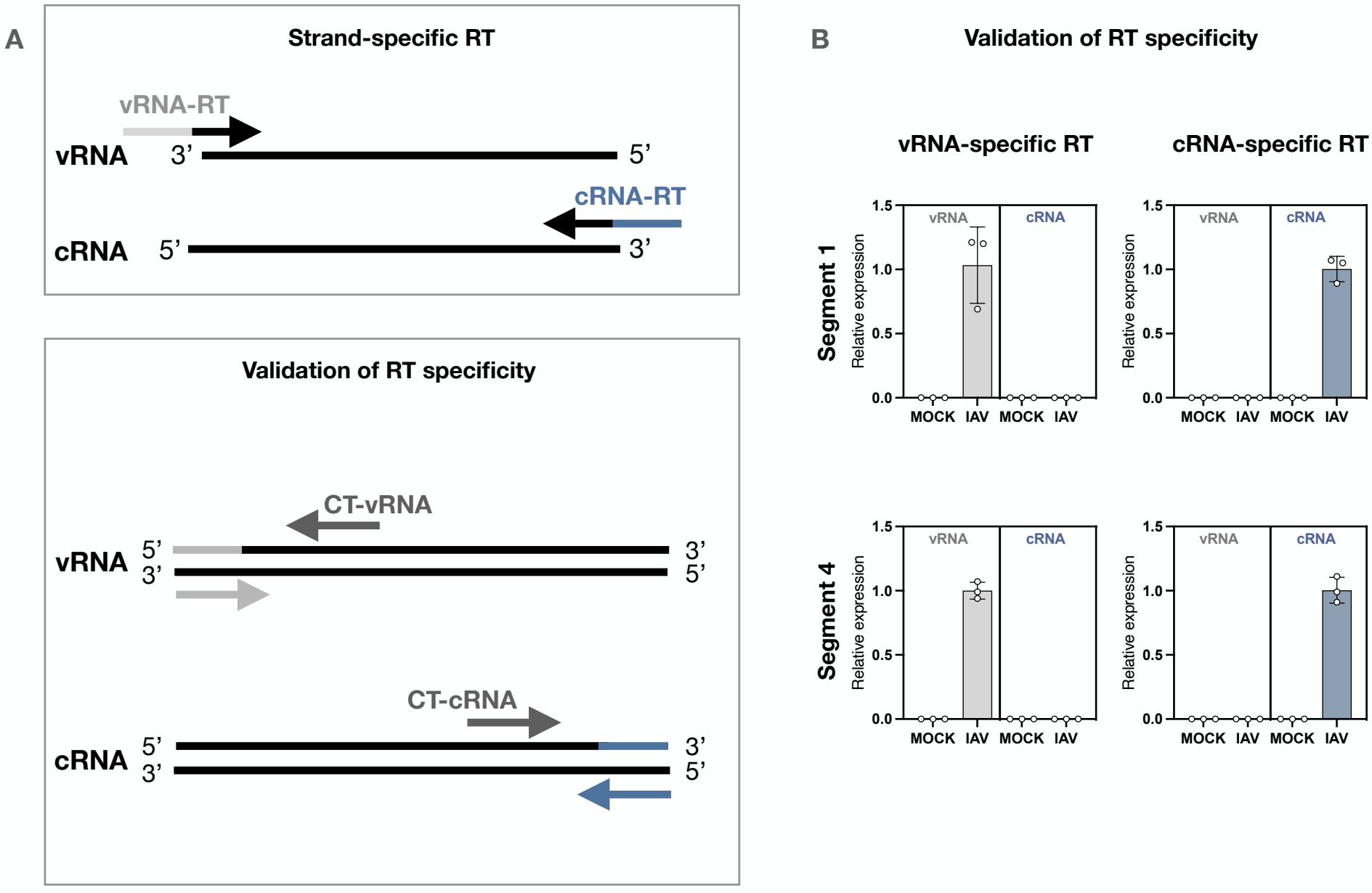

Supplemental Figure S3

Additionnal images for Figure 1G

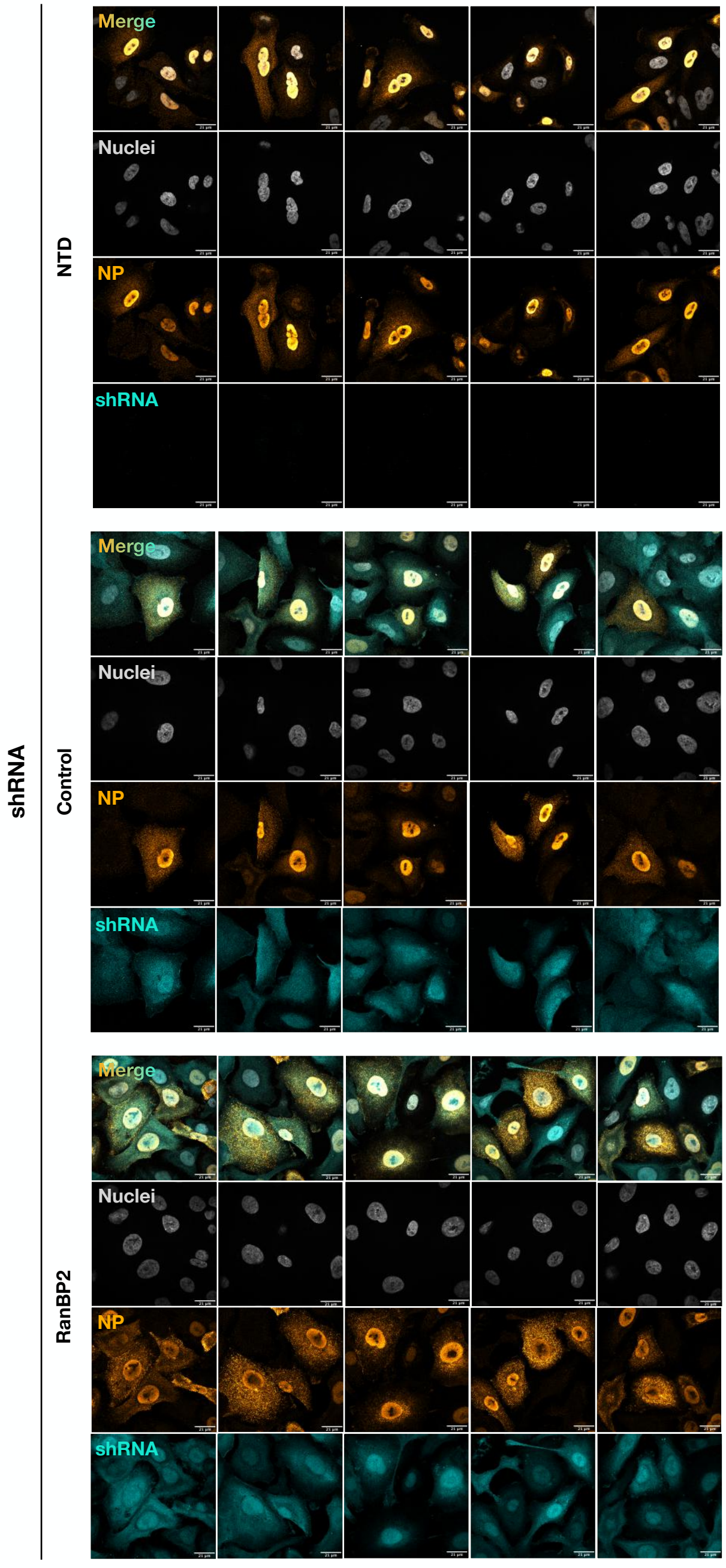

Supplemental Figure S4

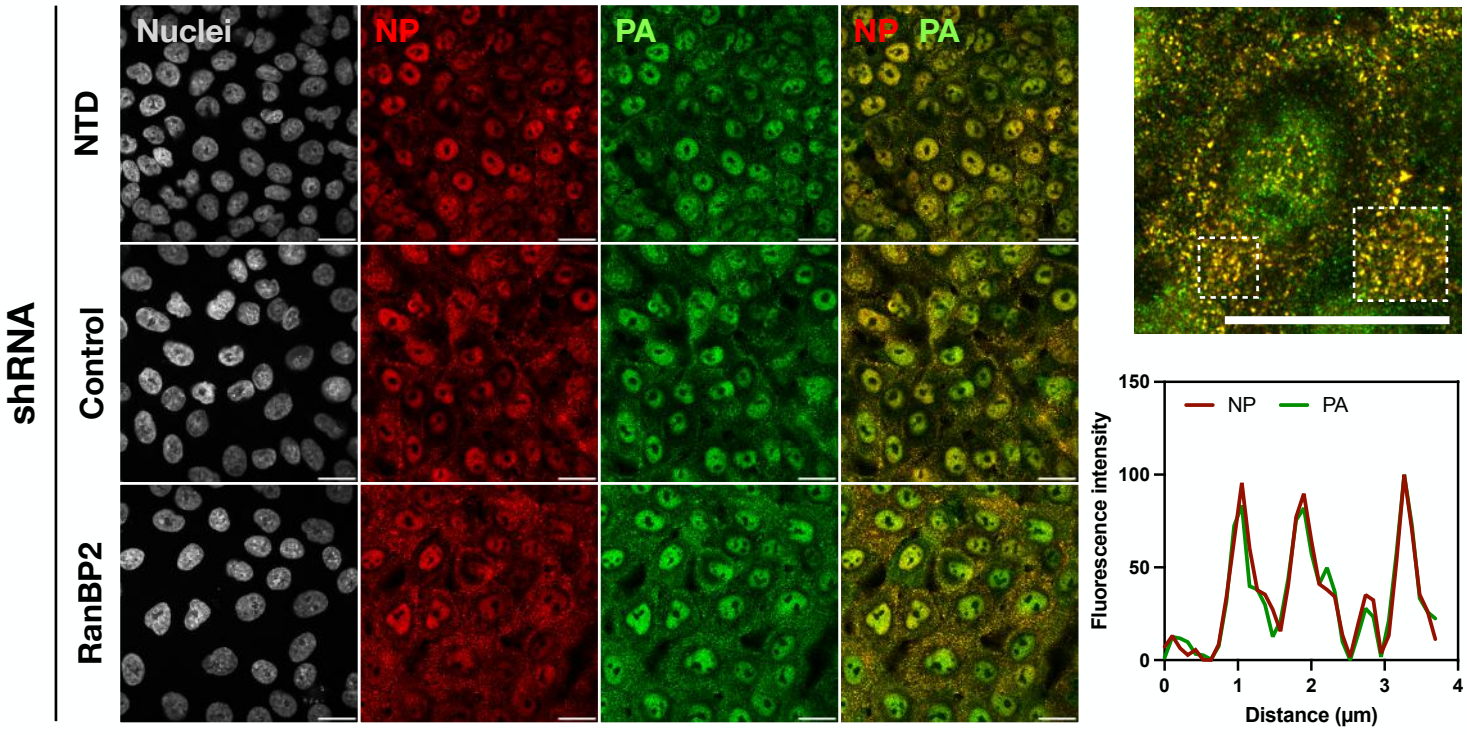

Supplemental Figure S5

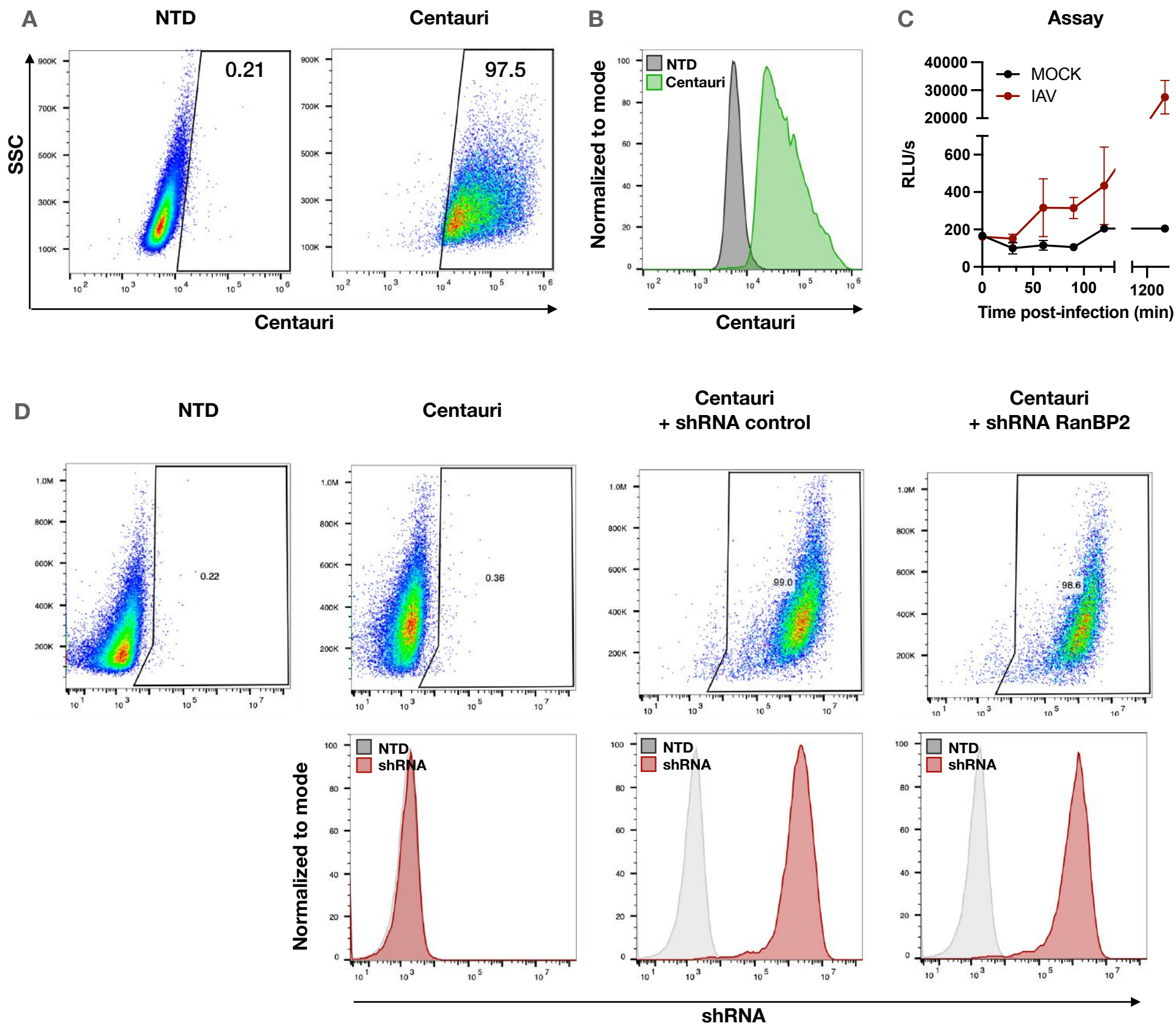

Supplemental Figure S6

A

Dose-response to KPT-330 (8 hpi)

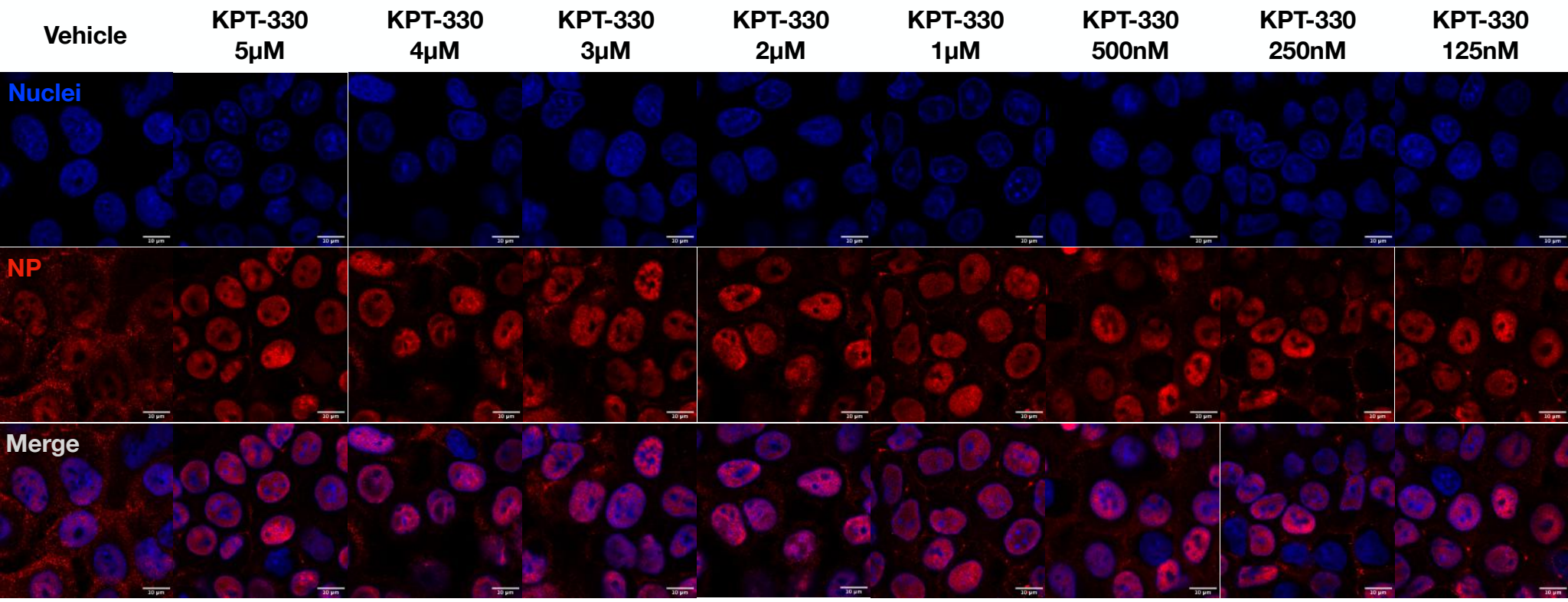

B

Viability

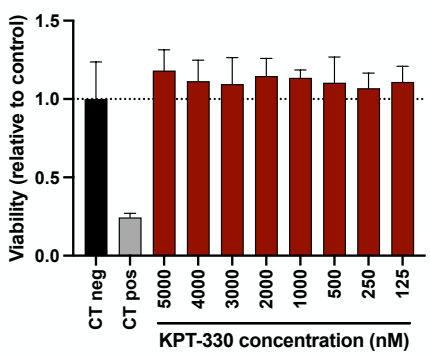

C

Time-response to KPT-330 (5μM)

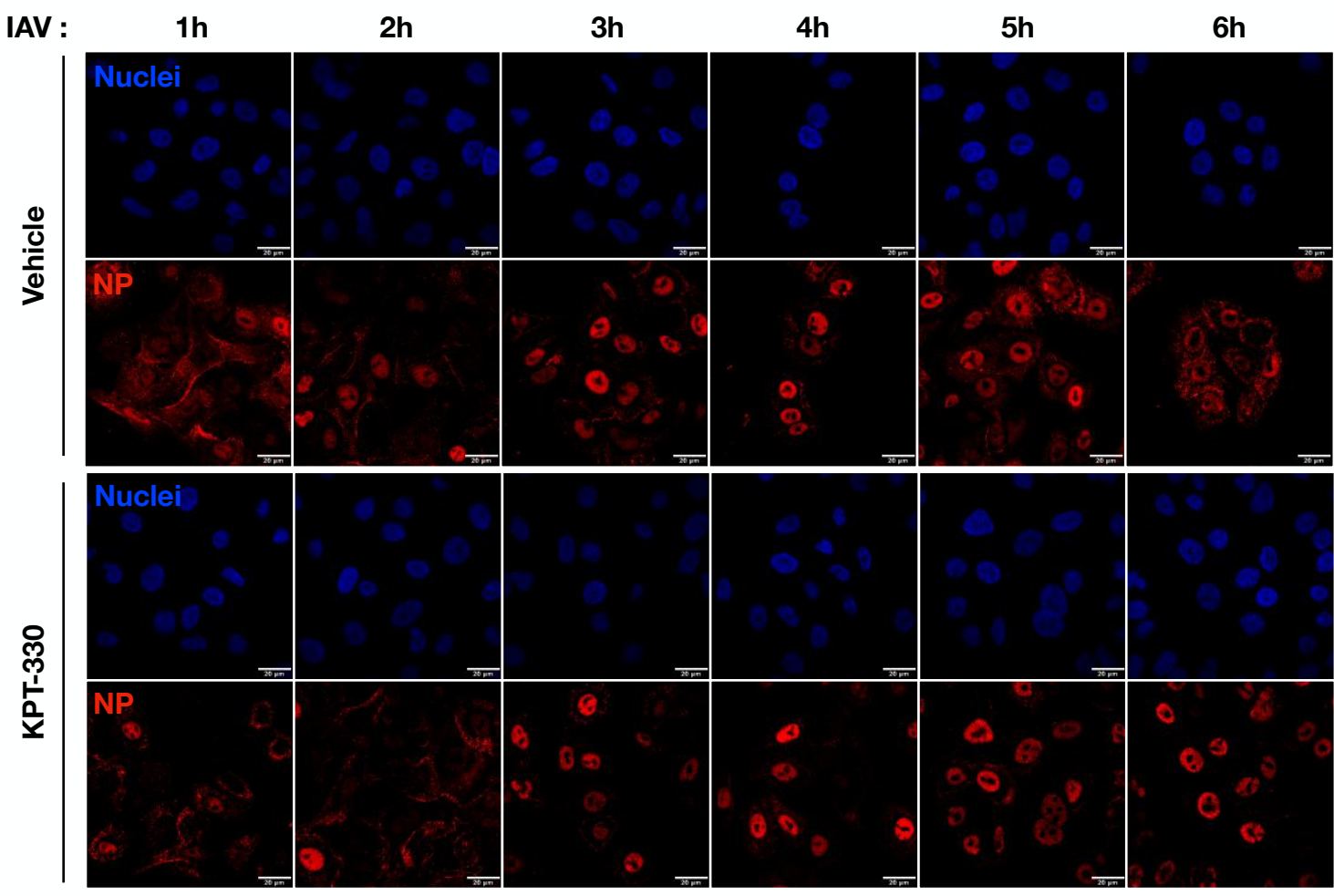

Supplemental Figure S7

Images for Figure 2D

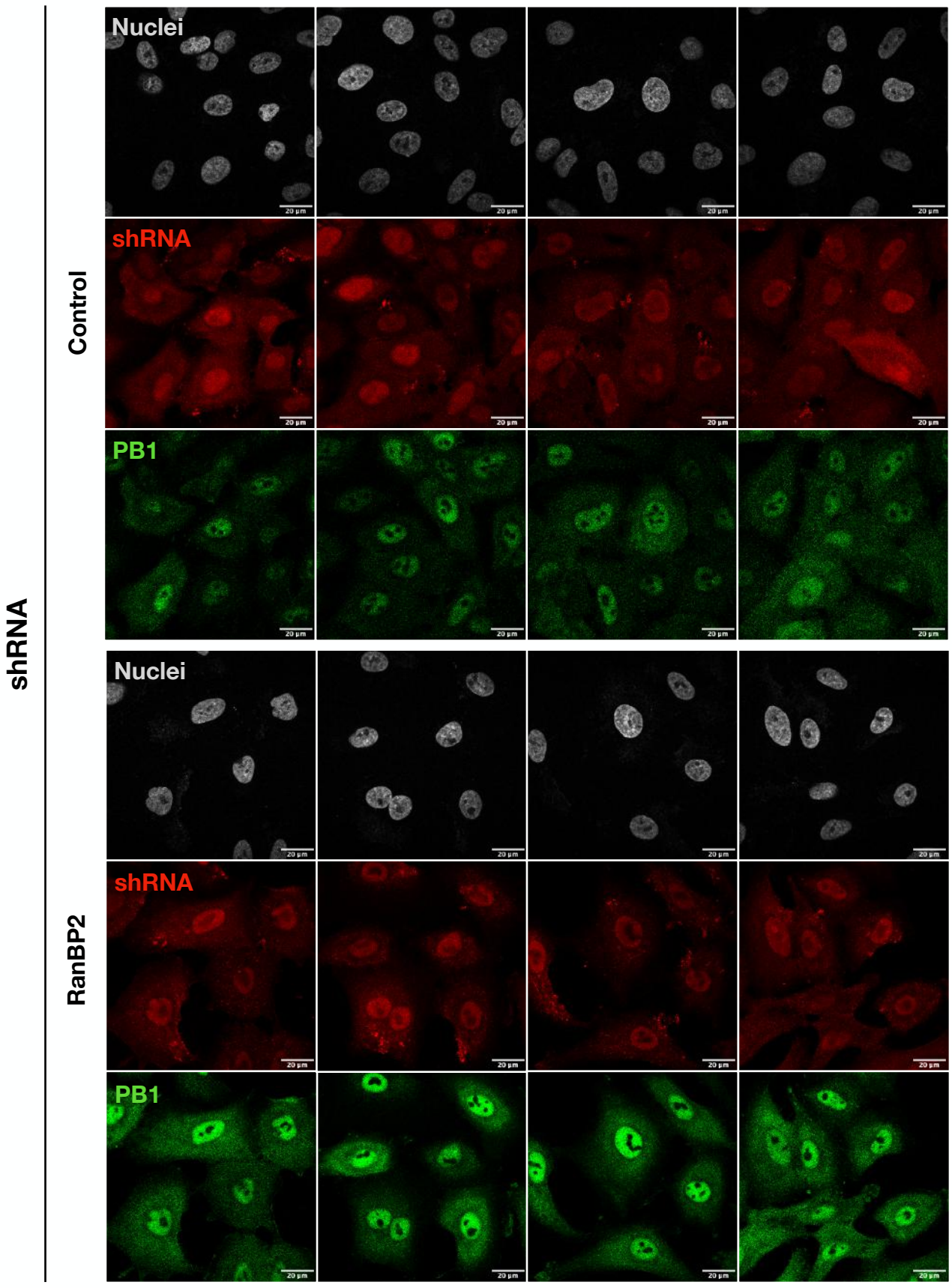

Supplemental Figure S8

A

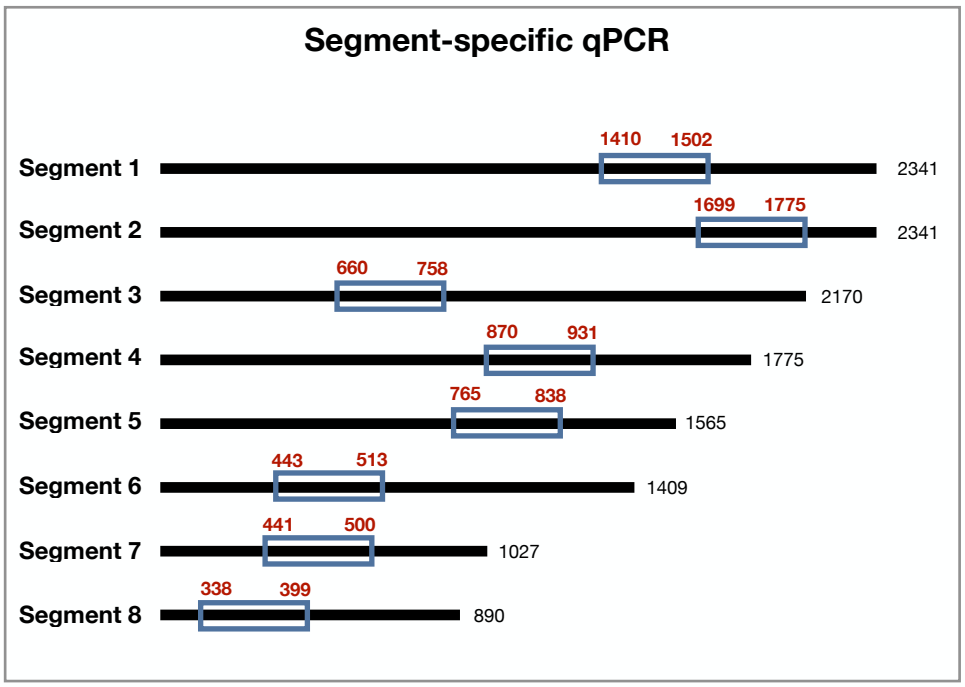

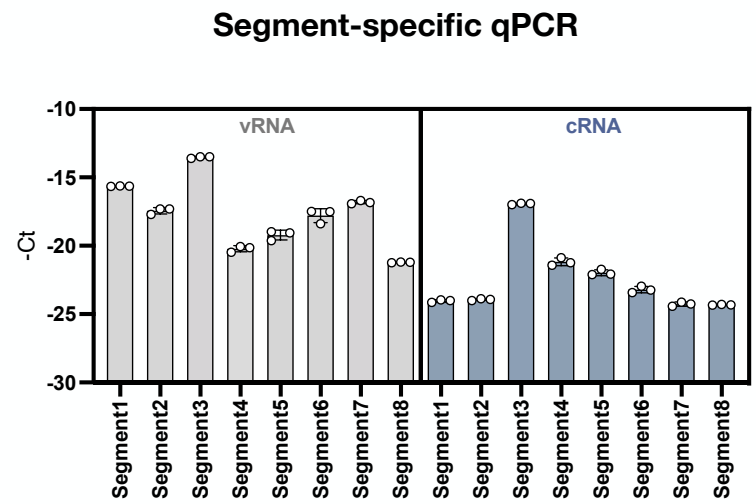

B

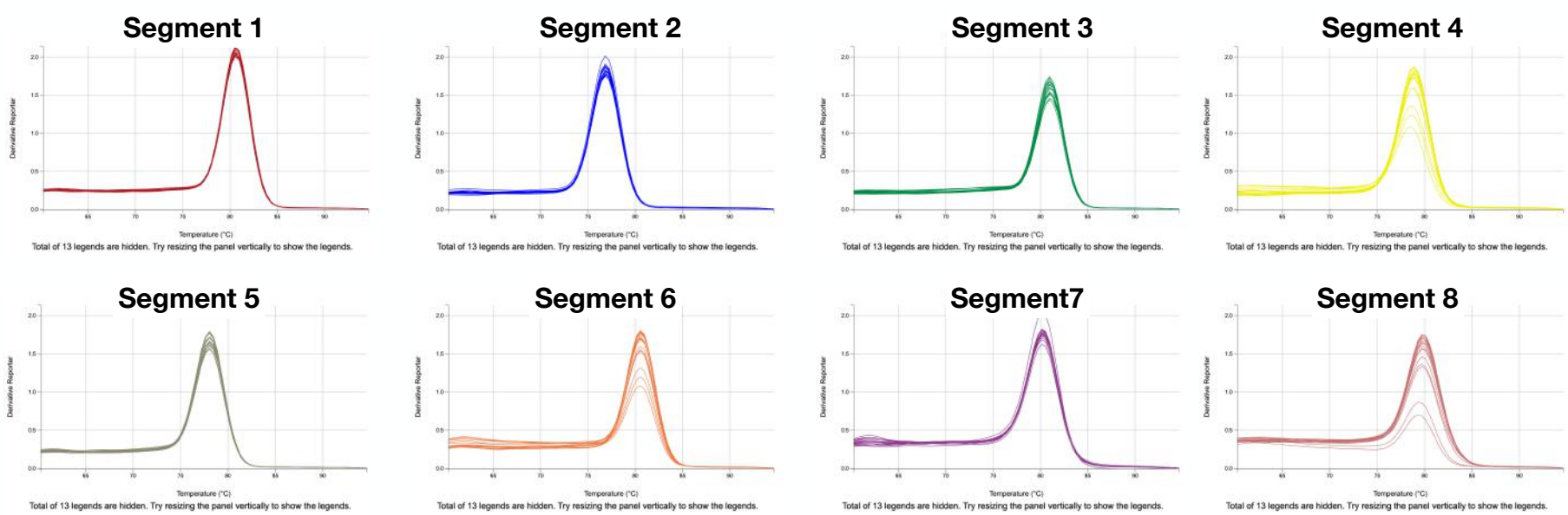

Supplemental Figure S9

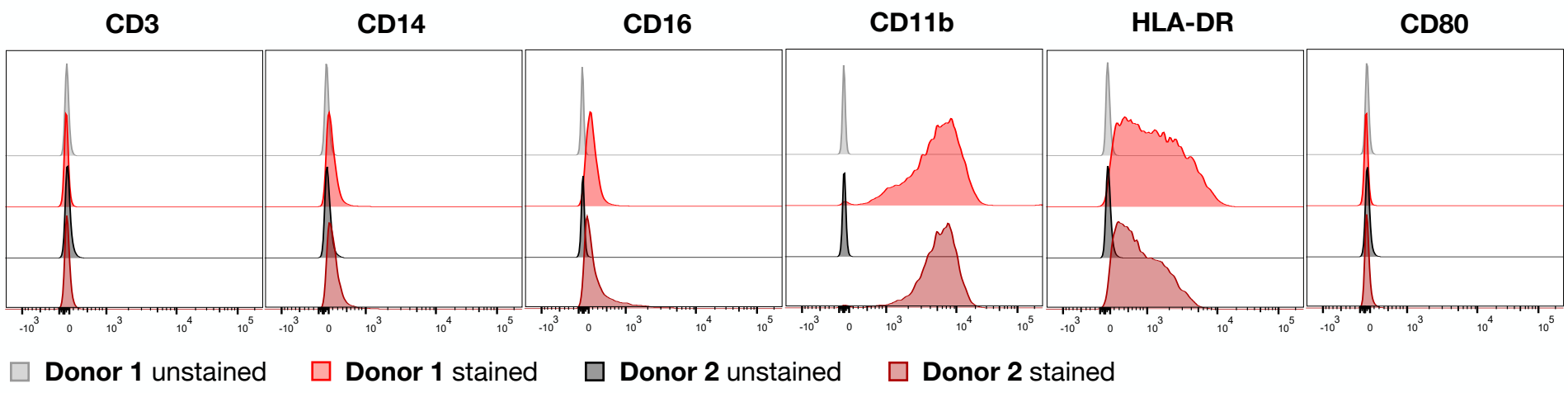

Supplemental Figure S10

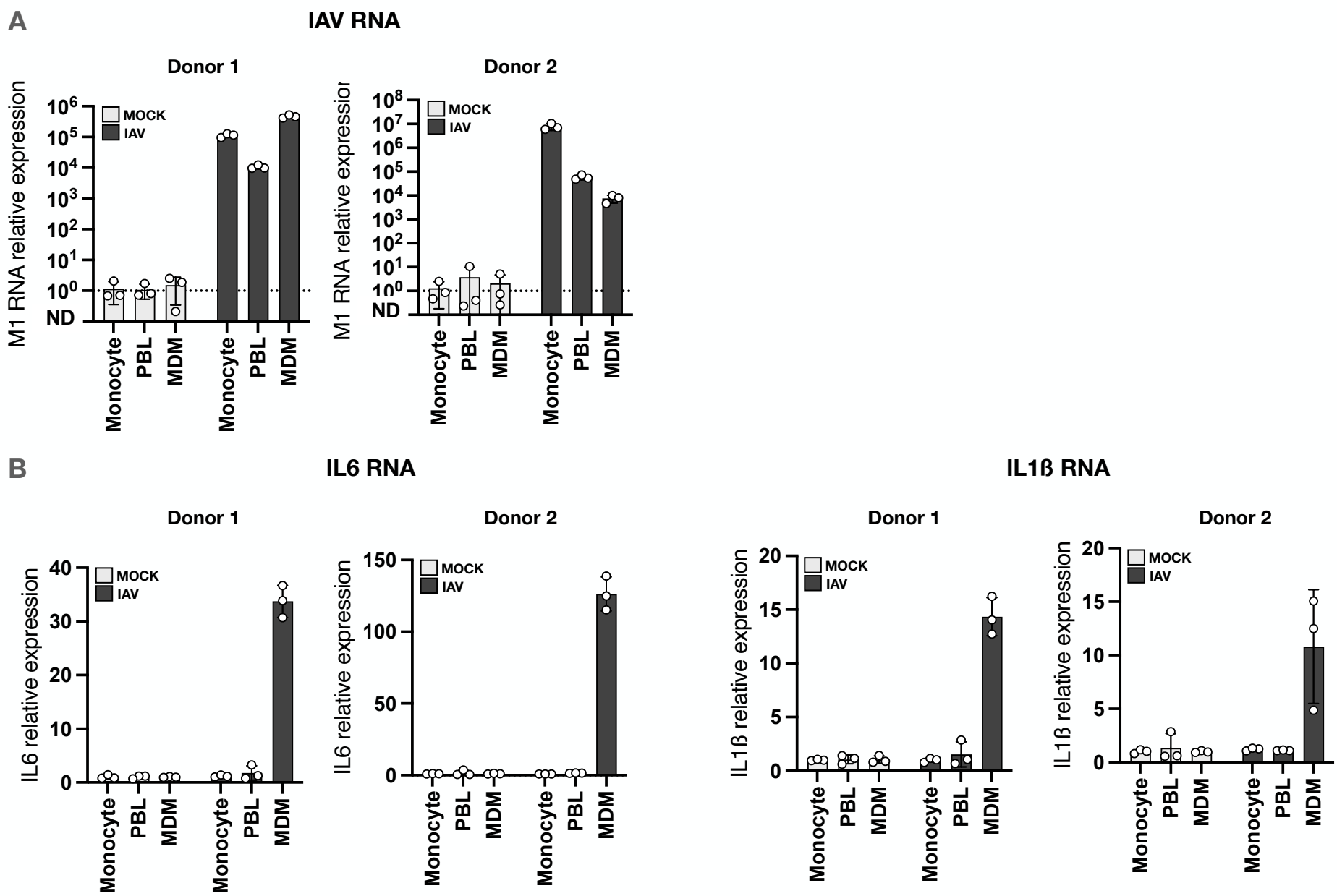

Supplemental Figure S11

A ***RANBP2*-specific allelic qPCR strategy**

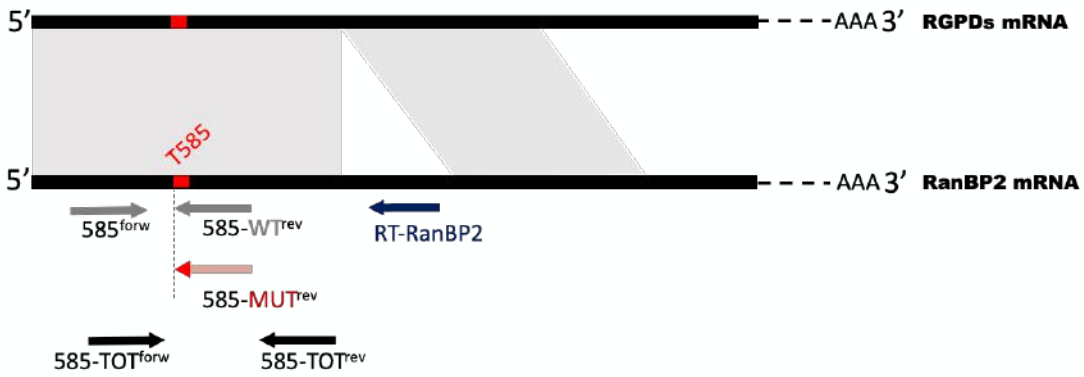

B **No recombination with RGPDs**

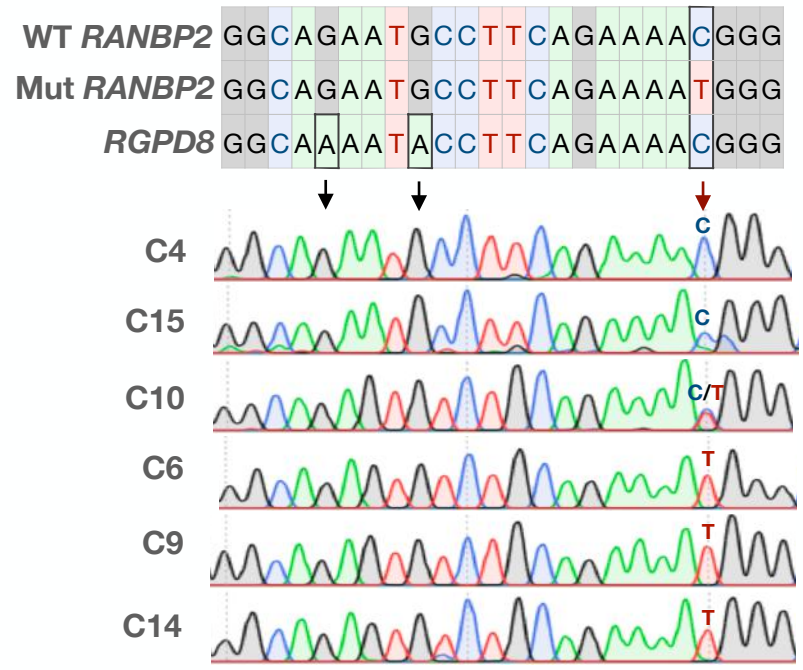

C **mCherry-cell sorting for allelic qPCR control cells**

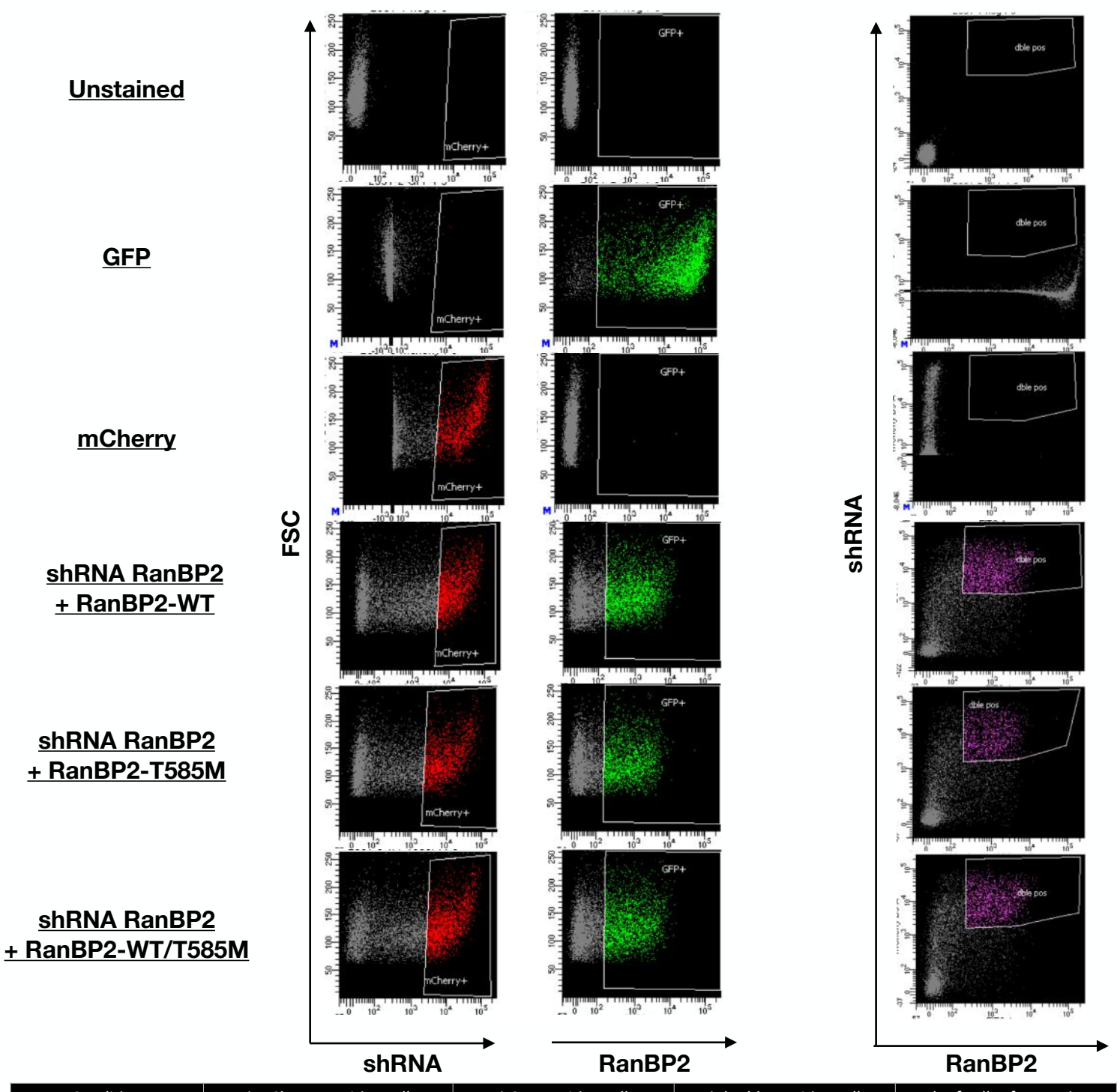

Condition	% mCherry-positive cells	% GFP-positive cells	% double-positive cells	Nb of cells after sorting
NTF	0	0	0	200000
GFP	0,1	90,9	0	N/A
mCherry	35,7	0	0	N/A
Ran + WT	25	37,4	24,8	106440
Ran + T585M	26,1	31,6	17,8	69272
Ran + WT/T585M	33,2	33,7	21,4	133453

Supplemental Figure S12

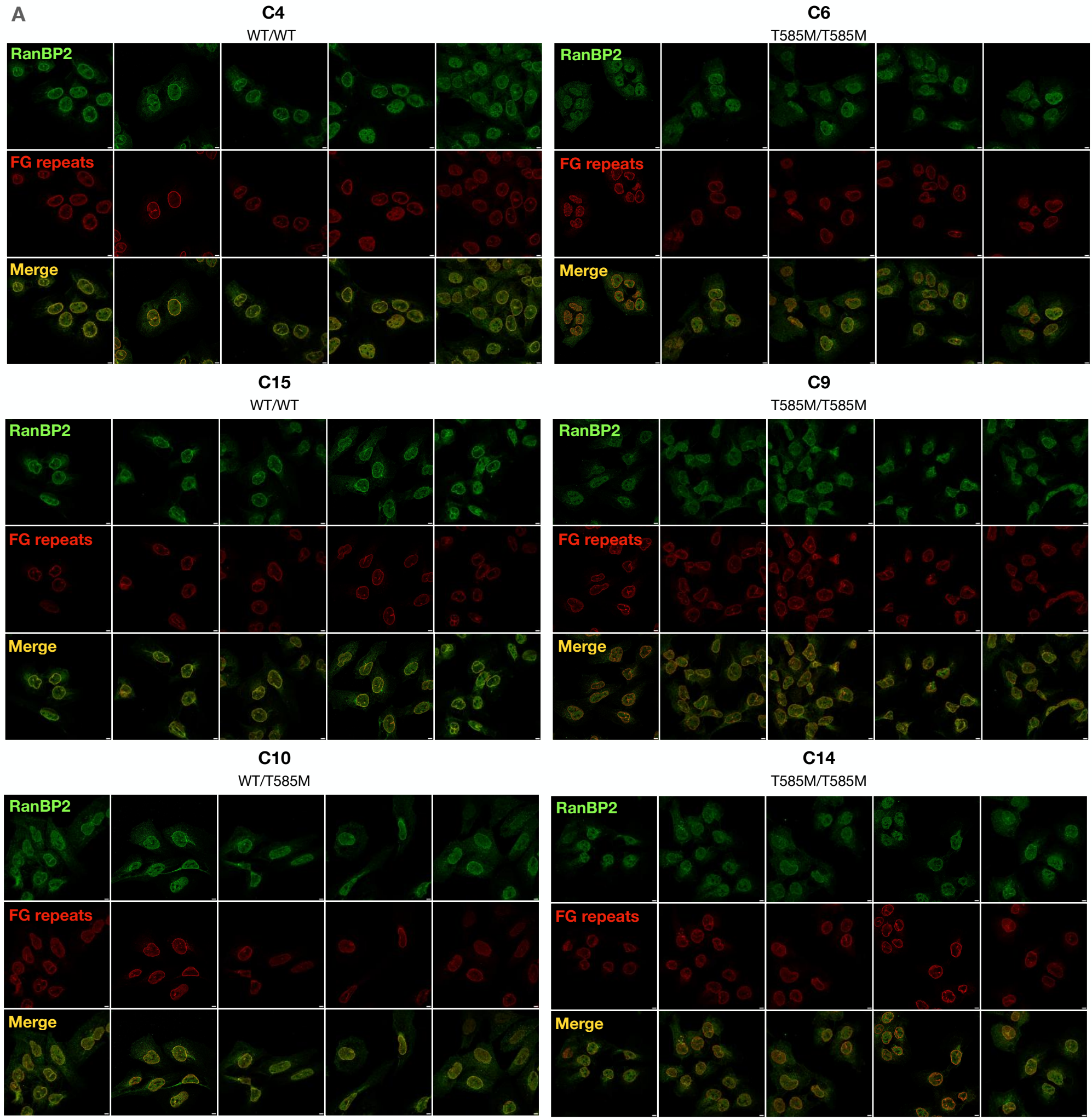

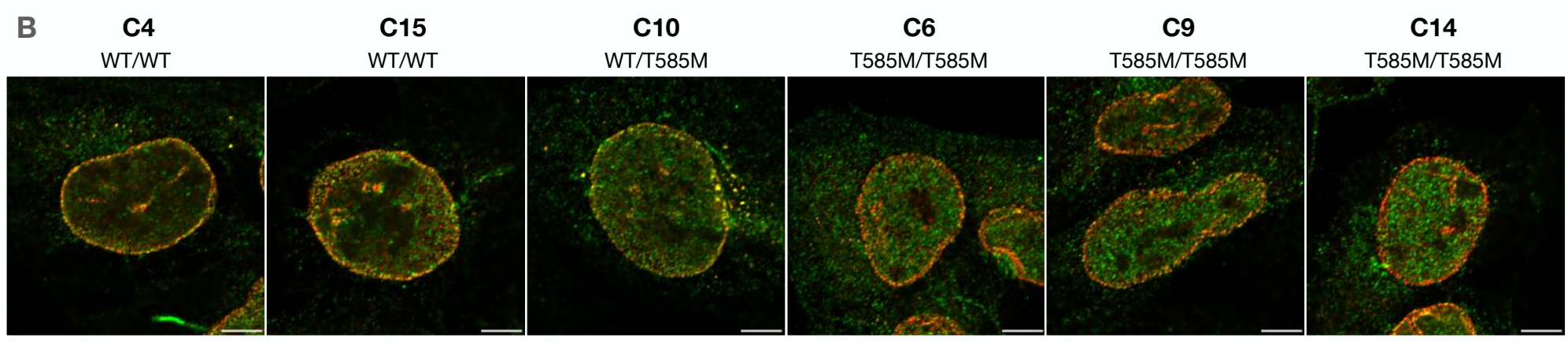

Table S1 **Plasmids**

Target	Reference
pVSVg	pHCMV-G (Yee et al., PNAS 1994)
p8.74	pCMVΔR8.74 (Dull et al., J Virol 1998)
mCherry-shRNA-Control	ddgene #1864 (Gouy et al., Front Neurol 2023)
mCherry-shRNA-RanBP2	Gouy et al., Front Neurol 2023
GFP-RanBP2-WT	Gift from J Joseph (Pune University)
GFP-RanBP2-T585M	This paper, availbale upon request
Centauri-Nluc-NLS	This paper, availbale upon request

Table S2 **Reverse transcription primers**

IAV strand-specific RT	
Target	Sequence (5' -> 3')
vRNA	GGCCGTCATGGTGGCGAATAGCGAAAGCAGG
cRNA	CCAGATCGTTCGAGTCGTAGTAGAAACAAGG

The colored sequence corresponds to the tag

RanBP2-specific RT	
Target	Sequence (5' -> 3')
RanBP2	ATGCTGTTGGGGTGGAAGCC

qPCR primers

Target	Forward primer (5'-3')	Reverse primer (5'-3')
IAV M1	CAGCACTGGAGCTAGGATGA	AAGGCTATGGAGCAAATGGC
IAV NP	CCTCGGGCCAAATCAGCATA	ATTCCCAGTGAATGCTGCCA
Segment 1	CGGGATATTGCCCGACATGA	TCCGCGCTGGAATACTCATC
Segment 2	TACCGGTGCCATAGAGGTGA	TGGGTTTGCTCCCACAGTTT
Segment 3	CAAGCTTGCCGACCAAAGTC	TTGCCCTCAATGTAGCCGTT
Segment 4	GGCATCATCACCTCAAACGC	CCCTGGGGTGTTTGACACTT
Segment 5	TCAAGTGAGAGAGAGCCGGA	TGAGTGCAGACCGTGCTAAA
Segment 6	TTAATGAGCTGCCCTGTCGG	GCTGACCAAGCAACCGATTC
Segment 7	CCACTGAAGTGGCATTTGGC	GCTGGGAGTCAGCAATCTGT
Segment 8	GCTCATGCCCAAGCAGAAAG	CCATGATCGCCTGGTCCATT
RanBP2 (Total)	AAAACATGGCCTTCAACCTG	TCAACAATTTCTGATGCCTGA
RanBP2 (WT)	TGGGATGCGGTTTGTACTCT	AGAATTAAGACCGCTGCCCG
RanBP2 (T585M)	TGGGATGCGGTTTGTACTCT	AGAATTAAGACCGCTGCCCA
RanBP2 (Exon24)	CAGGAAGCTCAAAAATCTCAGACA	ACCATCACTTCAGTCCCACC
IL-6	TAACCACCCCTGACCCAACC	ATTTGCCGAAGAGCCCTCAG
IL-1ß	GGCATCCAGCTACGAATCTC	GAACCAGCATCTTCCTCAGC
TNFα	GGCGTGGAGCTGAGAGATAAC	GGTGTGGGTGAGGAGCACAT
IL-18	GGAATTGTCTCCCAGTGCAT	ACTGGTTCAGCAGCCATCTT
CXCL10	GTCCACGTGTTGAGATCATTGC	TTGCTCCCCTCTGGTTTTAAGG
RPL13a	AACAGCTCATGAGGCTACGG	TGGGTCTTGAGGACCTCTGT
Actine B	CTGGAACGGTGAAGGTGACA	AAGGGACTTCCTGTAACAATGCA

Table S3 **Antibodies**

Immunofluorescence			
Target	Reference	Brand	Dilution
NP	MCA400	Biorad	1/1000
PB1	GTX125923	GeneTex	1/500
RANBP2	27606-1-AP	Proteintech	1/100
FG repeats NPC (clone mab414)	902901	Biolegend	1/200
Goat anti-Mouse AF488	A11001	Thermofisher Scientific	1/1000
Goat anti-Rabbit AF488	A11034	Thermofisher Scientific	1/1000
Goat anti-Mouse AF555	A21424	Thermofisher Scientific	1/1000

Flow cytometry and MDM phenotyping			
Target	Reference	Brand	Dilution
HA (Centauri)	11988506001	Roche, Sigma	1/100
CD3-BV421 (clone UCHT1	300433	Biolegend	1/100
CD14-PerCP-Cy5.5 (clone HCD14)	325621	Biolegend	1/100
CD16-Alexa700 (clone 3G8)	302026	Biolegend	1/100
CD11b-APC-Cy7 (clone M1/70)	101225	Biolegend	1/100
HLA-DR-FITC (REA805)	130-111-941	Miltenyi	1/100
CD80-BV650 (clone 2D10)	305227	Biolegend	1/100

Western Blot			
Target	Reference	Brand	Dilution
NP	MCA400	Biorad	1/5000
PB1	GTX125923	GeneTex	1/5000
PB2	GTX125925	GeneTex	1/5000
PA	GTX125932	GeneTex	1/5000
Pro-IL1ß	16806-1-AP	Proteintech	1/1000
NLRP3	AG-20B-0014	Adipogen	1/1000
Actin ß	A1978	Roche, Sigma	1/3000
Lamin A/C	10298-1-AP	Proteintech	1/400
Tubulin	ab6160	Abcam	1/5000
Goat anti-Mouse HRP	NA931V	GE Healthcare	1/5000
Donkey anti-rabbit HRP	NA934V	GE Healthcare	1/5000